Article

Targeting FSP1 triggers ferroptosis in lung cancer

https://doi.org/10.1038/s41586-025-09710-8

Received: 25 August 2024

Accepted: 6 October 2025

Published online: 05 November 2025

Open access

Check for updates

Katherine Wu[1,2,12], Alec J. Vaughan[1,2,12], Jozef P. Bossowski[1,3], Yuan Hao[1,3], Aikaterini Ziogou[1,3], Seon Min Kim[4], Tae Ha Kim[4], Mari N. Nakamura[1,3], Ray Pillai[1,5,6], Mariana Mancini[1,3], Sahith Rajalingam[1,3], Mingqi Han[7,8], Toshitaka Nakamura[9], Lidong Wang[10], Suckwoo Chung[1,3], Diane Simeone[10], David Shackelford[7,8], Yun Pyo Kang[4], Marcus Conrad[9,11] & Thales Papagiannakopoulos[1,3]✉

Emerging evidence indicates that cancer cells are susceptible to ferroptosis, a form of cell death that is triggered by uncontrolled lipid peroxidation[1–3]. Despite broad enthusiasm about harnessing ferroptosis as a novel anti-cancer strategy, whether ferroptosis is a barrier to tumorigenesis and can be leveraged therapeutically remains unknown[4,5]. Here, using genetically engineered mouse models of lung adenocarcinoma, we performed tumour-specific loss-of-function studies of two key ferroptosis suppressors, GPX4[6,7] and ferroptosis suppressor protein 1 (FSP1)[8,9], and observed increased lipid peroxidation and robust suppression of tumorigenesis, suggesting that lung tumours are highly sensitive to ferroptosis. Furthermore, across multiple pre-clinical models, we found that FSP1 was required for ferroptosis protection in vivo, but not in vitro, underscoring a heightened need to buffer lipid peroxidation under physiological conditions. Lipidomic analyses revealed that *Fsp1*-knockout tumours had an accumulation of lipid peroxides, and inhibition of ferroptosis with genetic, dietary or pharmacological approaches effectively restored the growth of *Fsp1*-knockout tumours in vivo. Unlike *GPX4*, expression of *FSP1* (also known as *AIFM2*) was prognostic for disease progression and poorer survival in patients with lung adenocarcinoma, highlighting its potential as a viable therapeutic target. To this end, we demonstrated that pharmacologic inhibition of FSP1 had significant therapeutic benefit in pre-clinical lung cancer models. Our studies highlight the importance of ferroptosis suppression in vivo and pave the way for FSP1 inhibition as a therapeutic strategy for patients with lung cancer.

Ferroptosis is a non-apoptotic, oxidative stress-dependent mechanism of cell death that is uniquely distinguished by lipid peroxidation of polyunsaturated fatty acids of membrane phospholipids (PUFA-PLs)[1,10]. Lipid peroxidation involves the formation of lipid and lipid peroxyl radicals, which, in auto-oxidative propagation reactions, generate lipid hydroperoxides. Aberrant, unrestricted lipid peroxidation results in altered membrane integrity, cell swelling, and ultimately membrane rupture[11,12]. In recent years, growing interest in ferroptosis has revealed that cells depend on several enzymes to protect against ferroptosis[6–9,13–15], of which GPX4 and FSP1 have key roles. GPX4 catalyses the reduction of PUFA-PL hydroperoxides to non-toxic alcohols. FSP1 catalyses the reduction of extramitochondrial coenzyme Q_{10} (CoQ), a highly potent lipid radical-trapping antioxidant (RTA). Conversely, cells can be sensitized to ferroptosis through PUFA-PL composition[16] and biosynthesis by ACSL4[17–19]. In addition to these cellular pathways, exogenous lipid RTAs, such as LIP1, FER1, vitamin E and vitamin K, have also been shown to specifically inhibit ferroptosis[1,6,20–22].

Emerging evidence indicates that cancer cells, including drug-resistant cells that have adopted a mesenchymal state[2,3], are highly sensitive to lipid peroxidation in vitro, suggesting a potential for harnessing ferroptosis as a novel anti-cancer strategy. Although there have been extensive studies characterizing GPX4 and more recently FSP1 in various diseases[4,23], whether ferroptosis constitutes a barrier to tumorigenesis and the functional roles of GPX4 and FSP1 in in vivo cancer models remain poorly characterized. To date, FSP1 has been shown to be a critical ferroptosis suppressor only in the absence of GPX4[8,9,24].

[1]Department of Pathology, New York University Grossman School of Medicine, New York, NY, USA. [2]Vilcek Institute of Graduate Biomedical Sciences, New York University Grossman School of Medicine, New York, NY, USA. [3]Laura and Isaac Perlmutter Cancer Center, New York University Langone Health, New York, NY, USA. [4]College of Pharmacy and Research Institute of Pharmaceutical Sciences, Seoul National University, Seoul, Korea. [5]Division of Pulmonary and Critical Care Medicine, Department of Medicine, VA New York Harbor Healthcare System, New York, NY, USA. [6]Division of Pulmonary, Critical Care, and Sleep Medicine, Department of Medicine, New York University Grossman School of Medicine, New York, NY, USA. [7]Pulmonary and Critical Care Medicine, David Geffen School of Medicine (DGSOM), University of California Los Angeles (UCLA), Los Angeles, CA, USA. [8]Jonsson Comprehensive Cancer Center, UCLA, Los Angeles, CA, USA. [9]Institute of Metabolism and Cell Death, Molecular Targets and Therapeutics Center, Helmholtz Munich, Neuherberg, Germany. [10]Moores Cancer Center, University of California, San Diego, La Jolla, CA, USA. [11]Translational Redox Biology, Technical University of Munich (TUM), TUM Natural School of Sciences, Garching, Germany. [12]These authors contributed equally: Katherine Wu, Alec J. Vaughan. ✉e-mail: thales.papagiannakopoulos@nyulangone.org

However, given the high toxicity, poor selectivity and low-to-limited bioavailability of GPX4 inhibitors in vivo[25,26], as well as the only recent development of FSP1 inhibitors, the majority of which do not have in vivo efficacy[9,24,27–30], much work remains to demonstrate that ferroptosis induction could indeed be a therapeutic strategy for cancer[5].

Here we show that genetic knockout of either *Gpx4* or *Fsp1* (also known as *Aifm2*) in genetically engineered mouse models (GEMMs) of autochthonous KRAS-driven lung adenocarcinoma (LUAD)[31–35] results in marked restriction of lung tumorigenesis. We demonstrate that disruption of FSP1, often considered a backup axis of ferroptosis suppression, is sufficient to trigger exhibit enhanced lipid peroxidation in lung tumours. We confirm that Fsp1 deletion across several human cancer cell lines with various oncogenic drivers, co-mutations and tissue lineages consistently lead to in vivo tumour restriction. As ferroptosis can be functionally defined as a modality of cell death resulting from increased lipid peroxides and rescued only with inhibitors of lipid peroxidation, we demonstrate that *Fsp1*-knockout ($Fsp1^{KO}$) tumours have increased oxidized PUFA-PLs and that administration of lipid RTAs, as well as genetic loss of *Acsl4*, effectively restores lung tumorigenesis. Finally, we report that FSP1 is upregulated as LUAD tumours progress and show that FSP1 inhibition suppresses tumour growth and prolongs survival in multiple pre-clinical cancer models. Thus, our work utilizes novel in vivo models to characterize and test ferroptosis induction, particularly via FSP1 perturbation, as a therapeutic approach for lung cancer.

GPX4 prevents ferroptosis in lung tumours

GPX4 is considered the primary mediator of ferroptosis suppression, and has been shown to be essential across multiple mouse and human cancer cell types[7,26,36,37]. Therefore, we sought to interrogate whether GPX4, and more broadly ferroptosis suppression, is a requirement for lung tumorigenesis in vivo. Using a well-established GEMM of LUAD ($Kras^{LSL\text{-}G12D/+}$;$Tp53^{fl/fl}$;$Rosa26^{LSL\text{-}Cas9/LSL\text{-}Cas9}$), we initiated $Kras^{G12D/+}$;$Tp53^{-/-}$ (KP) tumours by intratracheal delivery of lentiviruses expressing Cre recombinase and dual single guide RNAs (sgRNAs)[38] targeting *Gpx4* (sg*Gpx4*) or non-targeting control sgRNAs (sg*Neo*), enabling CRISPR–Cas9-mediated *Gpx4*-knockout ($Gpx4^{KO}$) or wild-type control tumours, respectively. Concurrently, we treated a cohort of mice with each tumour genotype with LIP1, a potent lipid RTA and ferroptosis inhibitor, throughout the entire course of tumorigenic progression (Fig. 1a). Tumour-specific *Gpx4* deletion (sg*Gpx4*) led to a significant decrease in lung tumour burden that was not observed in sg*Gpx4* tumour-bearing mice treated with LIP1 (Fig. 1b–d). Efficient *Gpx4* deletion was verified by immunohistochemistry, with less than 15% of tumours in the sg*Gpx4* group staining positive for GPX4 (Extended Data Fig. 1a). Immunohistochemistry for 4-hydroxy-2-noneal (4-HNE), a marker for lipid peroxidation in tissues[20] (Extended Data Fig. 1b), revealed significantly higher levels of lipid peroxidation in sg*Gpx4* tumours compared with control sg*Neo* lung tumours, which was blunted with LIP1 treatment (Fig. 1e,f).

Similar to our in vivo observations, CRISPR–Cas9-mediated $Gpx4^{KO}$ in KP LUAD cells resulted in a near complete loss of viability and clonogenicity that was fully rescued by the addition of LIP1 (Extended Data Fig. 1c). Targeted lipidomics to profile oxidized phosphatidylcholine and phosphatidylethanolamine species in KP LUAD cells treated with RSL3, a covalent GPX4 inhibitor and inducer of ferroptosis, revealed a higher abundance of oxidized phospholipids in RSL3-treated cells that was decreased in cells treated with concomitant LIP1 (Extended Data Fig. 1d). GPX4 overexpression in KP LUAD cells had no effect on cell viability or clonogenicity basally (Extended Data Fig. 1e), but did confer greater resistance to ferroptosis in vitro (Extended Data Fig. 1f). Similarly, supplementation of KP LUAD cells with sodium selenite (Na_2SeO_3) to increase translation of GPX4[39], a selenoprotein, resulted in a corresponding increase in GPX4 expression and enhanced ferroptosis resistance in vitro (Extended Data Fig. 1g). Together, these results demonstrate that GPX4 is essential for lung tumours to evade ferroptosis and provide evidence that ferroptosis induction may be an effective anti-cancer strategy.

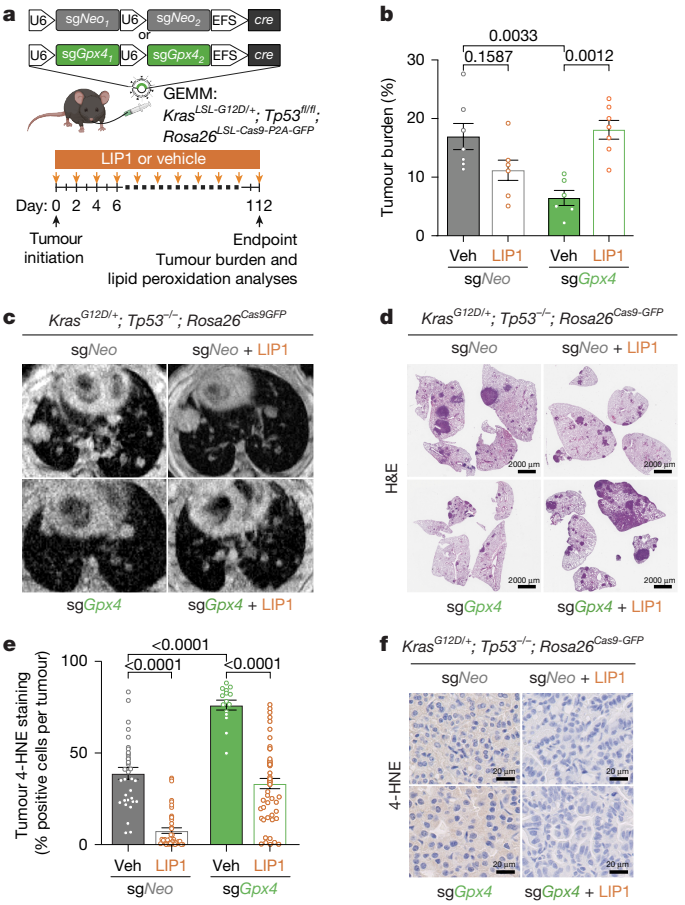

Fig. 1 | Gpx4 loss triggers ferroptosis in lung tumours. a, Schematic of KP LUAD GEMMs intratracheally infected with pUSEC lentiviruses containing dual sgRNAs targeting *Neo* (control; $n = 13$) or *Gpx4* ($n = 13$). Mice were dosed with LIP1 (sg*Neo*: $n = 6$, sg*Gpx4*: $n = 7$) or vehicle (sg*Neo*: $n = 7$, sg*Gpx4*: $n = 6$) every other day, starting from tumour initiation to experiment endpoint. **b**, Tumour burden of KP LUAD tumours with control (sg*Neo*) or *Gpx4* (sg*Gpx4*) knockout, treated with vehicle (Veh) or LIP1. **c**, Representative MRI of KP LUAD tumours with control (sg*Neo*) or *Gpx4* (sg*Gpx4*) knockout, treated with vehicle or LIP1. **d**, Representative haematoxylin and eosin (H&E) staining of KP LUAD tumours with control (sg*Neo*) or *Gpx4* (sg*Gpx4*) knockout, treated with vehicle or LIP1. Scale bars, 2,000 µm. **e**, Immunohistochemical detection of 4-HNE in KP LUAD tumours with control (sg*Neo*) or *Gpx4* (sg*Gpx4*) knockout, treated with vehicle or LIP1. **f**, Representative images of 4-HNE immunohistochemical staining from **e**. Scale bars, 20 µm. Data are mean ± s.e.m. One-way ANOVA with multiple comparisons (**b**,**e**). Drawing in **a** created in BioRender. Vaughan, A. (2025) https://BioRender.com/99qhixq.

FSP1 is upregulated in LUAD

Given our observation that GPX4 was required for lung tumorigenesis in a GEMM that closely recapitulates human LUAD development and progression, we next explored whether there was clinical evidence suggesting that ferroptosis regulators in general are altered in lung cancer[40]. Although GPX4 expression was modestly increased in *KRAS*-mutant LUAD tumours compared with normal lung tissue, there was no correlation with tumour stage or overall survival (Extended Data Fig. 1h,i). Concordantly, GPX4 protein levels also did not change during autochthonous LUAD progression in KP GEMM tumours (Extended Data Fig. 1j).

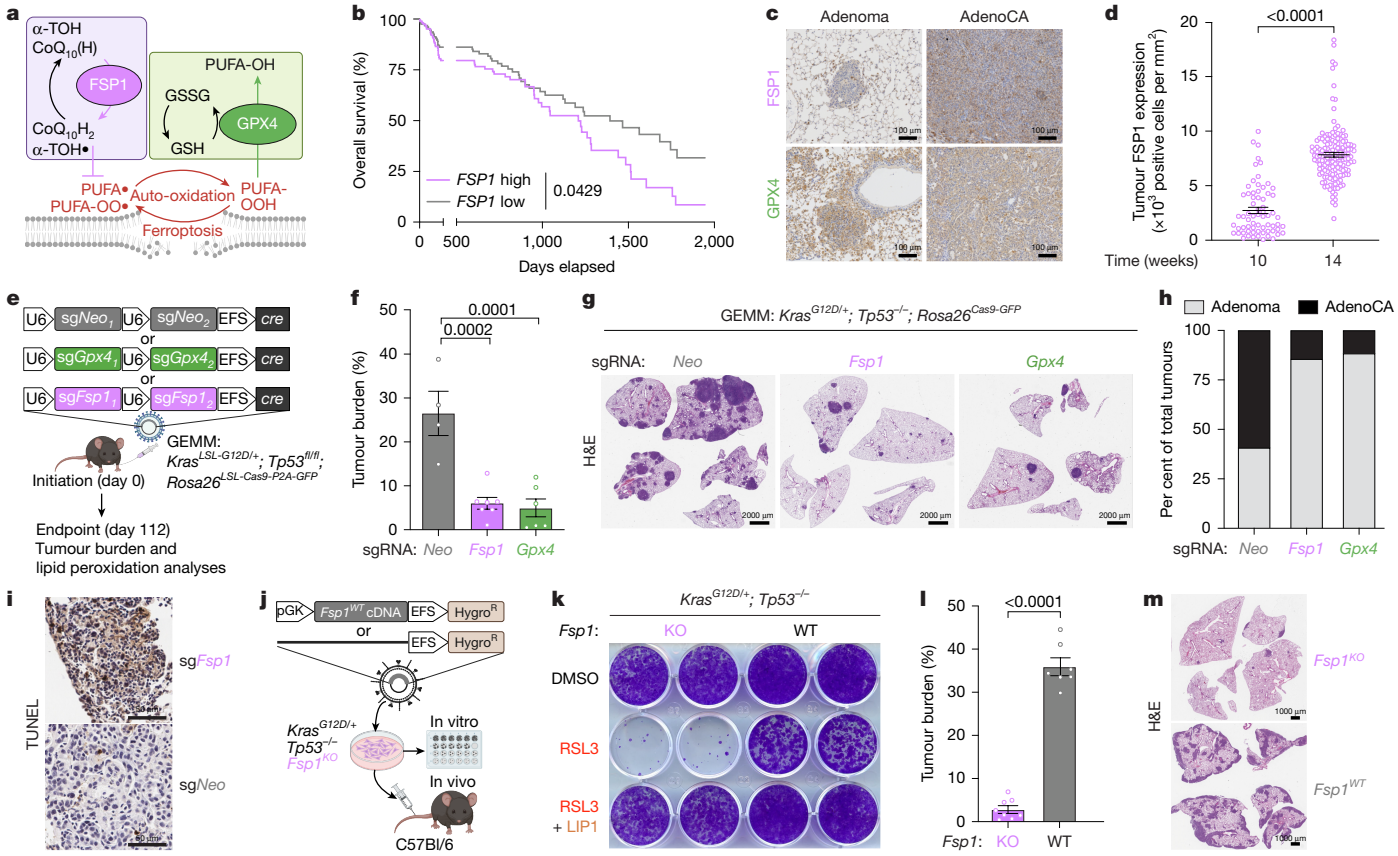

Fig. 2 | Fsp1 knockout robustly restricts lung tumorigenesis. a, Schematic depicting mechanisms of FSP1- and GPX4-mediated buffering against cellular lipid peroxidation and ferroptosis. GSH, reduced glutathione; GSSG, glutathoine disulfide; PUFA, polyunsaturated fatty acid; α-TOH, tocopherol (vitamin E). **b**, Overall survival of patients with *KRAS*-mutant LUAD ($n = 280$) from The Cancer Genome Atlas (TCGA), stratified by high versus low primary tumour *FSP1* expression. Median survival times for *FSP1*-high and *FSP1*-low tumours were 1,215 days and 1,498 days, respectively (hazard ratio 1.51 [1.01–2.25]). **c**, Representative immunohistochemistry for FSP1 and GPX4 in KP LUAD GEMM adenomas versus adenocarcinomas (AdenoCA). Scale bars, 100 µm. **d**, Immunohistochemical detection of FSP1 expression in KP LUAD GEMM tumours at 10 weeks and 14 weeks post-tumour initiation. **e**, Schematic of KP LUAD GEMMs intratracheally infected with pUSEC lentiviruses containing double sgRNAs targeting control (*Neo*; $n = 4$), *Fsp1* ($n = 7$) or *Gpx4* ($n = 6$). **f**, Tumour burden of KP LUAD tumours with knockout of either control (*Neo*), *Fsp1* or *Gpx4*. **g**, Representative H&E staining of KP LUAD tumours with knockout of either control (*Neo*), *Fsp1* or *Gpx4*. Scale bars, 2,000 µm. **h**, Relative proportion of KP adenomas and adenocarcinomas with knockout of either control (*Neo*), *Fsp1* or *Gpx4*. **i**, Representative TUNEL staining of KP, $Fsp1^{KO}$ and $Fsp1^{WT}$ orthotopic lung tumours. Scale bars, 50 µm **j**, Schematic depicting generation of isogenic $Fsp1^{WT}$ versus $Fsp1^{KO}$ cells for paralleled in vitro assays and in vivo syngeneic orthotopic transplantation studies. **k**, Representative images of crystal violet clonogenic growth assay in isogenic KP, $Fsp1^{KO}$ and $Fsp1^{WT}$ cells treated with RSL3 (0.5 µM) with or without LIP1 (100 nM). **l**, Tumour burden of KP, $Fsp1^{KO}$ ($n = 8$) and $Fsp1^{WT}$ ($n = 7$) orthotopic lung tumours. **m**, Representative H&E staining of KP, $Fsp1^{KO}$ and $Fsp1^{WT}$ orthotopic lung tumours. Scale bars, 2,000 µm. Data are mean ± s.e.m. Two-sided Student's *t*-test (**d**,**l**), one-way ANOVA with multiple comparisons (**f**) or Kaplan–Meier simple survival analysis (**b**). Drawings in **a**,**e**,**j** created in BioRender. Vaughan, A. (2025) https://BioRender.com/99qhixq.

Since GPX4 expression did not appear to correlate with any clinical prognostic factors in patients with *KRAS*-mutant LUAD, we next investigated FSP1, a second axis of ferroptosis surveillance (Fig. 2a). We found that FSP1 expression was robustly increased in tumours from patients with *KRAS*-mutant LUAD compared with normal lung, and exhibited a positive correlative trend with higher tumour stages (Extended Data Fig. 2a). Additionally, high FSP1 expression correlated with poor survival in patients with *KRAS*-mutant LUAD (Fig. 2b). Unlike GPX4, FSP1 protein levels increased temporally as lung tumours progressed from adenomas to adenocarcinomas in KP GEMMs (Fig. 2c,d). Together, these findings suggest that FSP1 may constitute a major suppressor of ferroptosis in LUAD and is potentially a more viable therapeutic target than GPX4 for patients with lung cancer.

Since prior studies have suggested that FSP1 may be regulated by KRAS signalling[41], to further determine whether FSP1 upregulation was specific to *KRAS*-mutant LUAD, we stratified patients with LUAD by major oncogenic mutations. Again, *FSP1* expression was robustly increased in tumours relative to normal lung tissue, and this upregulation was observed irrespective of driver mutation or *KRAS* variant (Extended Data Fig. 2b,c). Although *FSP1* expression was more robustly upregulated in *KRAS*-mutant tumours compared with *EGFR*-mutant tumours, LUAD tumours with neither mutation also exhibited upregulation of *FSP1* to the same extent as *KRAS*-mutant tumours. Next, we investigated whether the MAPK–ERK pathway regulates FSP1 expression. Both in vitro pathway inhibition with RMC-042, a pan-RAS inhibitor, in a panel of *KRAS*-mutant LUAD cell lines, as well as immunofluorescence of FSP1 and phosphorylated ERK in KP GEMM tumours revealed a lack of correlation between FSP1 expression and ERK activation (Extended Data Fig. 2d,e). Thus, these data indicate that *FSP1* expression, at least in the context of LUAD, may not be exclusively dependent on KRAS-mediated oncogenic signalling.

Given that patients with *KRAS*-mutant LUAD tumours often have concomitant mutations in *STK11* and *KEAP1*, which indicate more advanced disease and poorer prognosis[34,42], we also tested whether *FSP1* expression was impacted by these mutations. We observed that *FSP1* was significantly increased in LUAD tumours with co-mutation of either *STK11* or *KEAP1* (Extended Data Fig. 2f). Additionally, treatment of a panel of

human LUAD cell lines with the NRF2 activator KI696 led to significantly increased *FSP1* gene expression (Extended Data Fig. 2g). Of note, these findings are in accordance with recent studies that describe a role for NRF2, which is activated by *KEAP1* mutations, in FSP1 upregulation[43].

FSP1 is required for lung tumorigenesis

To systematically investigate the functional role of FSP1 in lung cancer, we initiated autochthonous KP LUAD tumours, this time with tumour-specific CRISPR–Cas9-mediated deletion of either *Fsp1* or *Gpx4* (Fig. 2e). Of note, we found that genetic deletion of *Fsp1* (sg*Fsp1*) in KP LUAD tumours strongly suppressed lung tumorigenesis, resulting in significantly decreased tumour burden to the same extent as $Gpx4^{KO}$ (sg*Gpx4*) tumours (Fig. 2f,g). Efficient Fsp1 deletion was verified by immunohistochemistry, with less than 5% of tumours in the in sg*Fsp1* group still staining positive for FSP1 (Extended Data Fig. 3a). We did not observe significant changes to the total number or size of tumours formed across the three biological groups (Extended Data Fig. 3b,c), which suggested that loss of *Fsp1* or *Gpx4* primarily affects tumour progression rather than tumour initiation. We also observed that *Fsp1* or *Gpx4* deletion resulted in higher proportions of adenomas to adenocarcinomas compared with control tumours (Fig. 2h), indicating that FSP1 and GPX4 are functionally important for malignant disease progression. Additionally, there were no notable changes to tumour cell proliferation or apoptotic cell death (Extended Data Fig. 3d,e) in sg*Fsp1* or sg*Gpx4* tumours. By contrast, TUNEL staining of lung tumours demonstrated increased cell death with loss of FSP1 (Fig. 2i), suggesting that the decreased lung tumour burden with *Fsp1* or *Gpx4* genetic deletion is likely to be due to increased tumour cell ferroptosis. Perhaps most notable is the extent to which *Fsp1* deletion phenocopied *Gpx4* loss in vivo, as this phenotype, to our knowledge, has not previously been reported in any other cell lines, tissues or disease models.

FSP1 is required uniquely in vivo

The identification of FSP1 as a key regulator of ferroptosis arose from genetic screens to identify ferroptosis suppressors in the absence of functional GPX4[8,9]. Thus, FSP1 is generally thought to control a secondary anti-ferroptotic axis whose function, at least in vitro, is masked when GPX4 is intact. Accordingly, we observed that CRISPR–Cas9-mediated *Fsp1* deletion in KP LUAD cells had no effect on cell viability and clonogenicity in vitro (Extended Data Fig. 4a). As expected, $Fsp1^{KO}$ cells were more sensitive to RSL3 treatment than isogenic *Fsp1*-wild-type ($Fsp1^{WT}$) cells and were protected from killing following RSL3 administration by LIP1 (Fig. 2k). Despite the remarkable restriction of KP LUAD tumorigenesis by *Fsp1* loss in vivo, our in vitro studies indicated that the anti-ferroptotic function of FSP1 was not required by KP LUAD cells in the presence of GPX4.

We sought to dissect this dichotomy and better understand the distinct in vivo dependency of lung tumours on FSP1. We first performed a series of syngeneic transplantation experiments using isogenic KP, $Fsp1^{KO}$ and $Fsp1^{WT}$ cell lines with no proliferation differences in vitro to systematically characterize the impact of FSP1 loss on tumour growth and further interrogate whether FSP1-mediated tumour differences were specific to in vivo growth conditions (Fig. 2j and Extended Data Fig. 4b). Consistently, we found that $Fsp1^{KO}$ cells formed significantly smaller tumours in both immunocompetent subcutaneous xenografts (Extended Data Fig. 4c,d) as well as orthotopic lung tumours (Fig. 2l,m and Extended Data Fig. 4e,f). Robust suppression of $Fsp1^{KO}$ orthotopic lung tumour growth was similarly observed in immunodeficient athymic (NU/J) mice (Extended Data Fig. 4g), as well as in an immunogenic mouse model[42] (Extended Data Fig. 4h). We also observed the same phenotype in age- and sex-matched $Fsp1^{WT}$ versus $Fsp1^{KO}$ mice (Extended Data Fig. 4i). These studies collectively provide strong evidence that the pro-tumorigenic effect of FSP1 is primarily cell intrinsic. *Fsp1* overexpression ($Fsp1^{OE}$) in KP LUAD cells exhibited no in vitro growth advantage (Extended Data Fig. 4j) but had enhanced resistance to killing by RSL3 (Extended Data Fig. 4k) and accelerated growth of xenograft tumours in vivo (Extended Data Fig. 4l,m). Altogether, these results suggest that FSP1 is essential for survival of LUAD cells in vivo and that increased FSP1 expression is sufficient to promote *Kras*-mutant tumorigenesis in vivo.

FSP1 dependency is not mutation-specific

To more thoroughly interrogate the functional importance of FSP1 for tumorigenesis and the translational potential for targeting FSP1 in cancer, we assessed the requirement of FSP1 for growth of xenograft tumours from human LUAD cell lines with a variety of driver mutations, including *KRAS*, *NRAS*, *EGFR*, *TP53*, *STK11* and *KEAP1*. We found that CRISPR–Cas9-mediated *FSP1* genetic deletion consistently and markedly decreased tumour growth in all models tested. Specifically, knockout of *FSP1* (sg*FSP1*) in H2009 (*KRAS*, *TP53* mutant), H1299 (*NRAS*, *TP53* mutant), PC9 and H1975 (*EGFR, TP53* mutant) LUAD cells led to robust suppression of subcutaneous tumour growth (Fig. 3a–d), but, analogous to aforementioned studies, did not affect proliferation or viability of cells in vitro unless they were treated with RSL3 (Extended Data Fig. 5a–d). To assess whether *KRAS*-mutant tumours with *STK11* (LKB1) and/or *KEAP1* mutations also depend on FSP1, we performed CRISPR–Cas9-mediated FSP1 deletion in A549 (*KRAS*, *KEAP1*, *STK11* mutant) and 16645 (*Kras* mutant, *Stk11*-null) LUAD cells. Again, we observed a dependency for FSP1 in vivo (Fig. 3e,f) but not in vitro (Extended Data Fig. 5e,f). Together these data provide further evidence that FSP1 is indeed required for in vivo LUAD tumour growth irrespective of driver and co-mutations.

Finally, we tested whether KRAS-driven tumours of a different lineage also exhibited a requirement for FSP1 in vivo. Transplantation of pancreatic adenocarcinoma (PDAC) *Kras*, *Tp53* mutant (KPC7) cells with CRISPR–Cas9-mediated *Fsp1* deletion also led to a robust tumour suppression in vivo (Fig. 3g and Extended Data Fig. 5g), mirroring the phenotype observed consistently in LUAD models and suggesting that FSP1 dependency in vivo may extend to other tissue lineages.

Ferroptosis inhibition rescues Fsp1 loss

We hypothesized that defective regulation of lipid peroxidation and subsequent induction of ferroptosis was the mechanism underlying $Fsp1^{KO}$ tumorigenic suppression. To assess this, we first performed epilipidomic analysis of $Fsp1^{WT}$ and $Fsp1^{KO}$ orthotopic lung tumours and observed that $Fsp1^{KO}$ tumours exhibited increased abundance of oxidized and truncated phosphatidylcholine and phosphatidylethanolamine species, indicative of increased cellular lipid peroxidation (Fig. 4a). We then explored whether ectopic overexpression of FSP1 or GPX4 (Extended Data Fig. 6a,b) was sufficient to restore the growth of $Gpx4^{KO}$ or $Fsp1^{KO}$ tumours, which would shed light on the capacity for each ferroptosis defence arm to compensate for the loss of the other. Indeed, we found that overexpression of FSP1 and GPX4 effectively restored the growth of $Gpx4^{KO}$ and $Fsp1^{KO}$ tumours, respectively (Fig. 4b,c and Extended Data Fig. 6c,d). These data implicated that tumours require extensive buffering capacity against lipid peroxidation, and that although GPX4 and FSP1 act through distinct pathways, each can compensate for the loss of the other.

Mechanistically, FSP1 has been shown to suppress ferroptosis by reducing the endogenous RTA CoQ, and this function is dependent on its localization to the plasma membrane. We utilized a liquid chromatography–mass spectrometry (LC–MS)-based, quantitative method to determine the abundance of CoQ in tumours, which revealed that $Fsp1^{KO}$ tumours had a significantly decreased ratio of reduced CoQ_9H_2 to oxidized CoQ_9 (Fig. 4d). This decreased ratio was not present in genotypically matched cells at baseline in vitro, but upon treatment

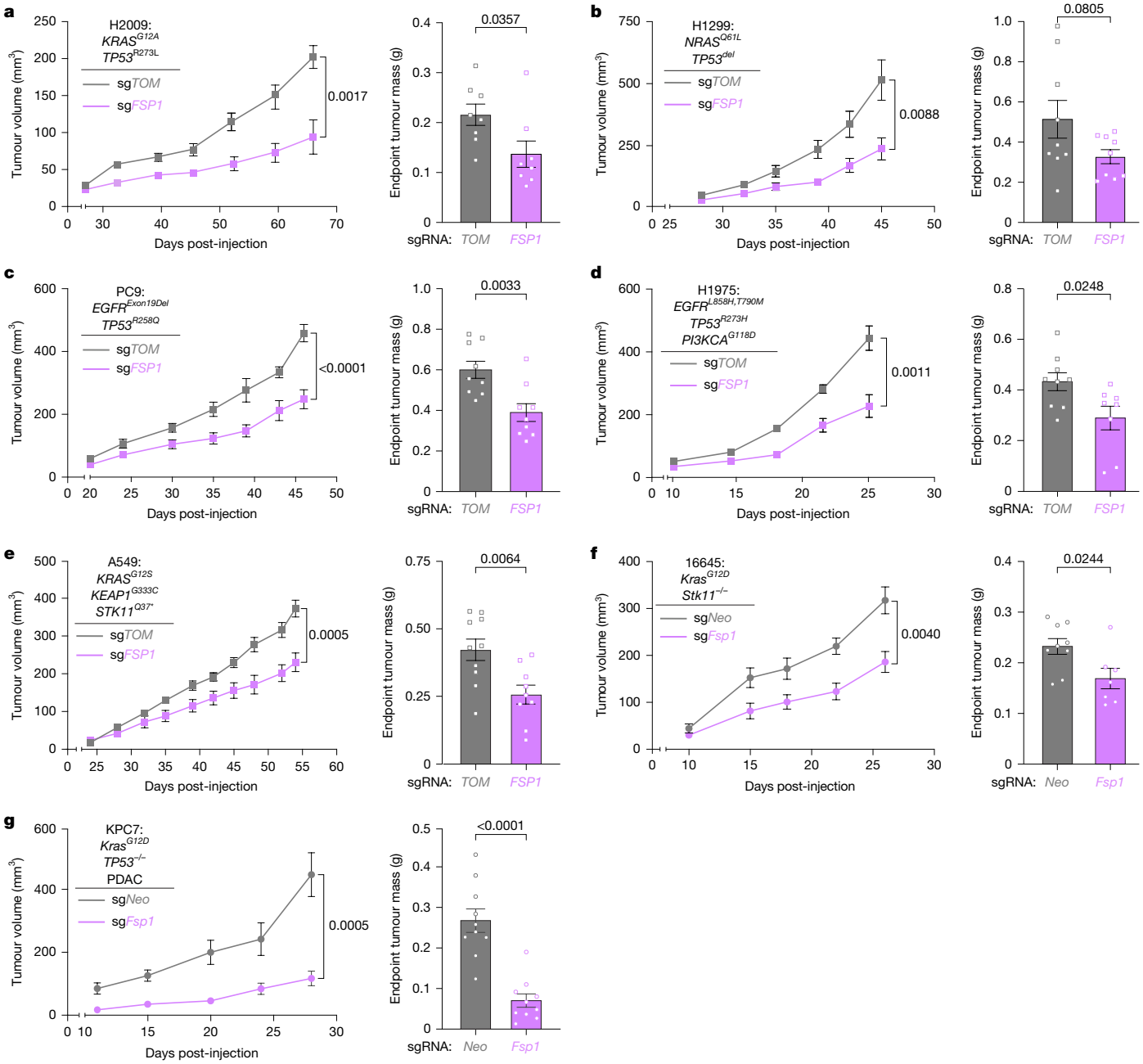

Fig. 3 | Sensitivity to FSP1 loss is not dependent on tumour mutations or lineage. a–**g**, Longitudinal tumour growth and endpoint tumour mass from indicated cell lines with CRISPR–Cas9-mediated knockout of FSP1 (sg*FSP1*) or control (sg*TOM*, sg*Neo*), transplanted as subcutaneous xenograft tumours into NSG mice. **a**, H2009 cells. sg*FSP1*: $n = 8$, control: $n = 8$. **b**, H1299 cells. sg*FSP1*: $n = 9$, control: $n = 9$. **c**, PC9 cells. sg*FSP1*: $n = 9$, control: $n = 9$. **d**, H1975 cells. sg*FSP1*: $n = 8$, control: $n = 9$. **e**, A549 cells. sg*FSP1*: $n = 9$, control: $n = 10$. **f**, 16645 cells. sg*Fsp1*: $n = 7$, control: $n = 9$. **g**, KPC7 (mouse PDAC cells). sg*Fsp1*: $n = 9$, control: $n = 10$. Data are mean ± s.e.m. Two-sided Student's *t*-test (**a**–**g**).

with RSL3, $Fsp1^{KO}$ cells mimicked the decreased CoQ_9H_2/CoQ_9 observed in tumours. Previous studies have described that mutation of the myristoylation sequence that targets FSP1 to the plasma membrane renders FSP1 unable to protect against lipid peroxidation in vitro[8,9], which we also observed in KP LUAD cells (Extended Data Fig. 6e,f). We anticipated that expression of this mutant FSP1 ($Fsp1^{mut}$) would be similarly unable to restore $Fsp1^{KO}$ tumour growth. Indeed, whereas $Fsp1^{WT}$-restored tumours grew quickly, $Fsp1^{mut}$ and $Fsp1^{KO}$ tumours exhibited decreased growth (Extended Data Fig. 6g). These data suggest that tumours require Fsp1 enzymatic activity and subcellular localization in vivo to specifically buffer against ferroptosis.

Next, we explored whether ferroptosis suppression, using several orthogonal approaches including tumour-specific *Acsl4* knockout, dietary vitamin E supplementation and LIP1 treatment would restore $Fsp1^{KO}$ tumour growth. Loss or inhibition of ACSL4, which limits the supply of PUFA-PL and restricts lipid peroxidation (Fig. 4e), has previously been shown to be protective against ferroptosis in $Gpx4^{KO}$ cells in vitro[17–19]. We therefore sought to determine whether genetic deletion of *Acsl4* would suppress ferroptosis and rescue the growth of $Fsp1^{KO}$ tumours in vivo. We performed CRISPR–Cas9-mediated genetic deletion of *Acsl4* (sg*Acsl4*) in isogenic KP, $Fsp1^{KO}$ and $Fsp1^{WT}$ cells. We observed that loss of *Acsl4* did not affect cell viability but robustly rescued RSL3-induced ferroptosis in vitro, in both $Fsp1^{WT}$ and $Fsp1^{KO}$ cells (Extended Data Fig. 6h). Of note, *Acsl4* deletion significantly restored $Fsp1^{KO}$ lung tumour growth in vivo (Extended Data Fig. 6i) and mice with *Acsl4*- and *Fsp1*-double-knockout tumours were found to have

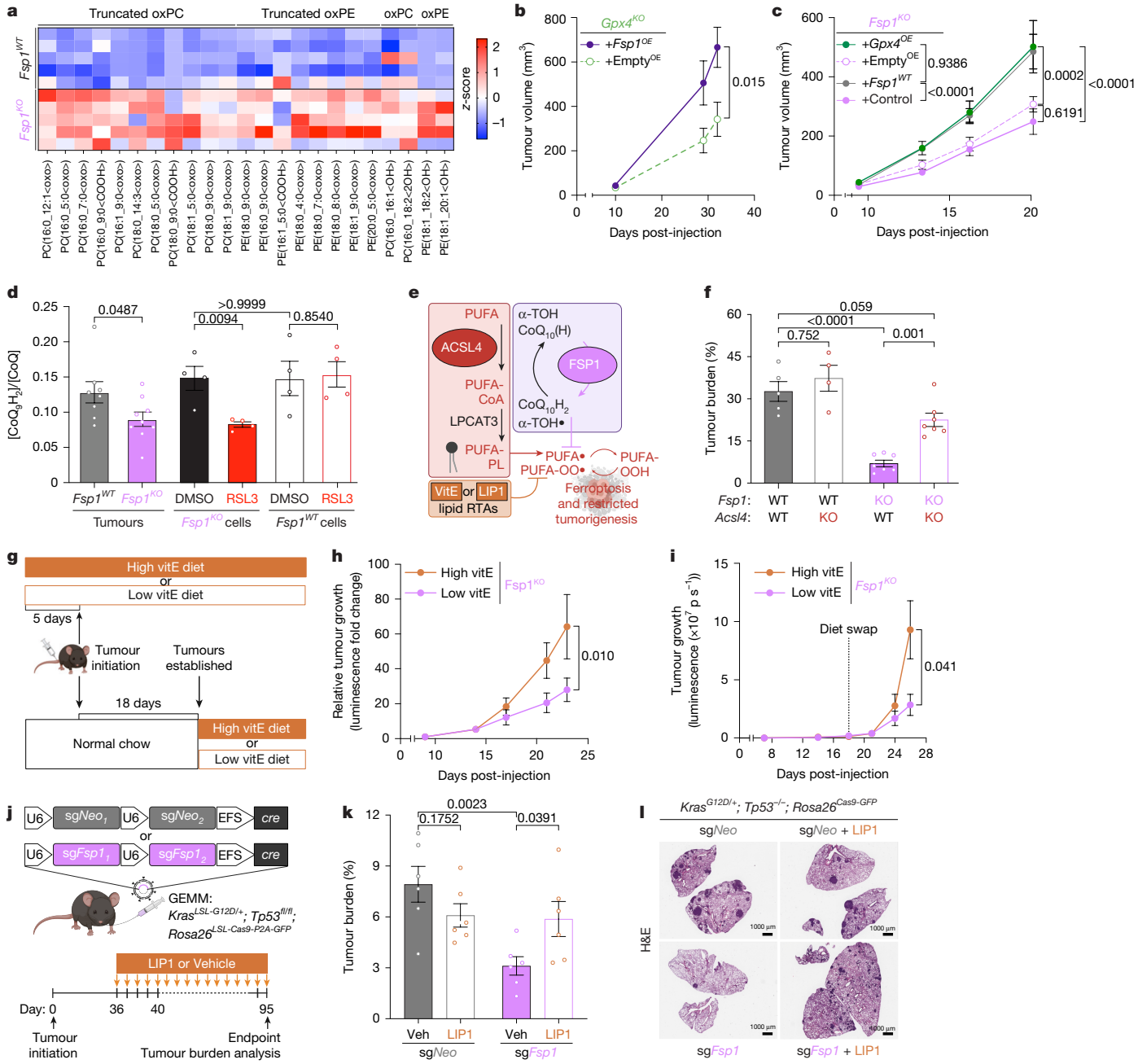

Fig. 4 | FSP1 is required for the suppression of ferroptosis in vivo. a, Heat map of indicated oxidized phosphatidylethanolamine (oxPE) and oxidized phosphatidylcholine (oxPC) lipid species detected via LC–MS from KP, *Fsp1*^{KO} and *Fsp1*^{WT} orthotopic lung tumours. **b**, Longitudinal growth of KP, *Gpx4*^{KO} subcutaneous xenograft tumours with *Fsp1*^{OE} ($n = 10$) versus control (empty vector (empty^{OE}); $n = 9$) in C57BL/6 J mice. **c**, Longitudinal growth of KP, *Fsp1*^{KO} subcutaneous xenograft tumours with either *Fsp1* restoration (*Fsp1*^{WT}, $n = 9$), GPX4 overexpression (*Gpx4*^{OE}; $n = 8$) or controls (empty^{OE}: $n = 9$; *Fsp1*^{KO}: $n = 8$) in C57BL/6 J mice. **d**, Ratio of CoQ_9H_2/CoQ_9 detected via LC–MS in KP, *Fsp1*^{KO} and *Fsp1*^{WT} orthotopic lung tumours and cells treated with DMSO or RSL3 (0.5 µM) for 8 h. **e**, Schematic depicting the pro-ferroptotic function of ACSL4. VitE, vitamin E. **f**, Tumour burden in C57BL/6 J mice with KP, *Fsp1*^{KO} and *Fsp1*^{WT} orthotopic lung tumours with CRISPR–Cas9-mediated *Acsl4* or control (Neo) deletion (wild type: $n = 5$, *Acsl4*^{KO}: $n = 4$, *Fsp1*^{KO}: $n = 7$, *Fsp1*^{KO}Acsl4^{KO}: $n = 7$). **g**, Schematic depicting dietary vitamin E manipulation studies in **h**,**i**. **h**, Longitudinal lung tumour growth (measured via bioluminescence normalized to first timepoint) in C57BL/6 J mice orthotopically transplanted with KP, *Fsp1*^{KO} cells and receiving high ($n = 8$) or low ($n = 7$) vitamin E diets ad libitum 5 days before tumour initiation. **i**, Longitudinal lung tumour growth (measured via bioluminescence) in C57BL/6 J mice orthotopically transplanted with KP, *Fsp1*^{KO} cells and placed on high ($n = 6$) or low ($n = 6$) vitamin E diets ad libitum on day 18 after tumour establishment. **j**, Schematic of KP LUAD GEMMs intratracheally infected with pUSEC lentiviruses containing double sgRNAs targeting *Neo* (control; $n = 12$) or *Fsp1* ($n = 12$). Mice were dosed with LIP1 ($n = 6$ per genotype) or vehicle ($n = 6$ per genotype) daily starting 5 weeks after tumour initiation. **k**, Tumour burden of mice described in **j**. **l**, Representative H&E staining of tumours from experiment in **j**. Scale bars, 100 µm. Data are mean ± s.e.m. Two-sided Student's *t*-test (**b**,**d**,**f**,**h**,**i**,**k**) or two-way ANOVA with Tukey's multiple comparison test (**c**). Drawings in **e**,**g**,**j** created in BioRender. Vaughan, A. (2025) https://BioRender.com/99qhixq.

increased endpoint disease burden (Fig. 4f and Extended Data Fig. 6j) and decreased overall survival (Extended Data Fig. 6k). Furthermore, tumour-specific knockout of *Acsl4* led to a basal acceleration of tumour growth (Extended Data Fig. 6i) and decreased overall survival (Extended Data Fig. 6k), suggesting that decreased accumulation of PUFA-PL in lung tumours may also protect against ferroptosis in vivo.

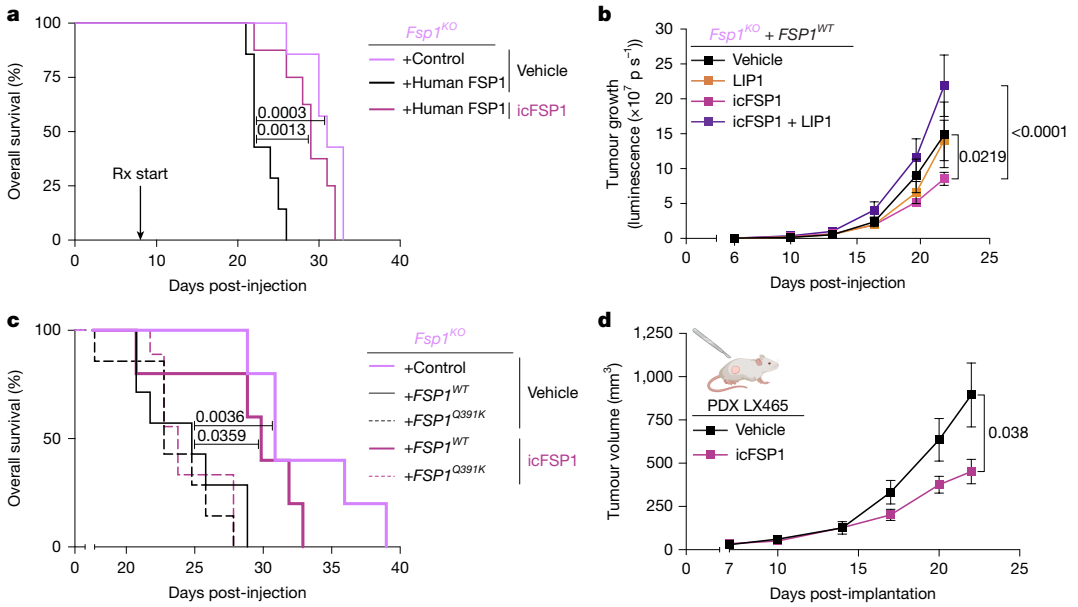

Fig. 5 | FSP1 is a viable therapeutic target for *KRAS*-mutant LUAD. a, Overall survival of C57BL/6 J mice with orthotopic lung tumours with *Fsp1*^{KO} ($n = 7$) or re-expression of human FSP1, treated with either icFSP1 ($n = 8$) or vehicle ($n = 7$). **b**, Longitudinal lung tumour growth (measured via bioluminescence) in C57BL/6 J mice orthotopically transplanted with *FSP1*^{WT} cells and treated with either vehicle ($n = 8$), LIP1 ($n = 7$), icFSP1 ($n = 8$) or icFSP1 plus LIP1 ($n = 8$). **c**, Overall survival of C57BL/6 J mice with *Fsp1*^{KO} ($n = 5$) tumours expressing wild-type human FSP1 (*FSP1*^{WT}) or human FSP1(Q319K) (*FSP1*^{Q319K}), treated with icFSP1 (*FSP1*^{WT}: $n = 5$, *FSP1*^{Q319K}: $n = 7$) or vehicle (*FSP1*^{WT}: $n = 7$; *FSP1*^{Q319K}: $n = 7$). **d**, Longitudinal growth of PDX LX465 tumours treated with icFSP1 ($n = 10$) or vehicle ($n = 10$) in NSG mice. Data are mean ± s.e.m. Two-way ANOVA with Tukey's multiple comparisons test (**b**), two-sided Student's *t*-test (**d**) or Kaplan–Meier simple survival analysis (**a**,**c**). Drawing in **d** created in BioRender. Vaughan, A. (2025) https://BioRender.com/99qhixq.

Vitamin E is nature's primary lipophilic antioxidant and is specifically able to scavenge lipid radicals and protect against ferroptosis (Fig. 4e). Therefore, we tested whether dietary vitamin E supplementation could rescue the growth of *Fsp1*^{KO} lung tumours. Mice were fed diets that were high or low in vitamin E ad libitum either before or after tumour initiation (Fig. 4g). We found that increased dietary vitamin E accelerated *Fsp1*^{KO} tumour growth (Fig. 4h,i), with no effect on growth of *Fsp1*^{WT} tumours (Extended Data Fig. 6l).

Finally, since LIP1 suppressed tumour lipid peroxidation and entirely mitigated the impact of *Gpx4* loss on KP LUAD tumorigenesis (Fig. 1b–d), we conducted parallel studies to investigate whether LIP1 also blunts ferroptosis in and restores *Fsp1*^{KO} tumorigenesis. In the orthotopic lung tumour model, we observed a tendency for *Fsp1*^{KO} tumours to grow more quickly with daily LIP1 administration (Extended Data Fig. 6m). In the KP LUAD GEMM (Extended Data Fig. 6n), which was conducted in accordance with experimental parameters for *Gpx4*^{KO} GEMM studies, LIP1 treatment significantly increased autochthonous *Fsp1*^{KO} (sg*Fsp1*) tumour burden (Extended Data Fig. 6o). Moreover, sg*Fsp1* tumours stained positively for 4-HNE, which was effectively suppressed by LIP1 treatment (Extended Data Fig. 6p). As observed with vitamin E supplementation, timing of LIP1 treatment did not appear to have a differential impact, as LIP1 treatment after tumours were already established was equally effective at restoring sg*Fsp1* lung tumorigenesis (Fig. 4j–l). Together, these studies provide clear evidence that LUAD tumours require FSP1 to protect against ferroptosis in vivo and suggest that increased lipid peroxidation is a barrier for tumour growth and progression.

FSP1 inhibition extends overall survival

As a result of the growing interest in harnessing ferroptosis to kill tumour cells, several FSP1 inhibitors have been developed[9,28], although the majority are effective only in vitro against human FSP1 in the context of GPX4 loss or inhibition (Extended Data Fig. 7a–d). icFSP1 was recently developed as the first inhibitor of human FSP1 with in vivo stability and efficacy, albeit solely in tumours with concomitant GPX4 loss[24]. Accordingly, we observed that icFSP1 treatment of KP LUAD cells in vitro did not affect cell viability (Extended Data Fig. 7e) unless RSL3 was added (Extended Data Fig. 7f). Given that mouse and human FSP1 are highly conserved in sequence and structure, we generated a hybrid tumour model in which human FSP1 was expressed in mouse KP, *Fsp1*^{KO} tumours. We observed that expression of either mouse or human FSP1 resulted in similar acceleration of tumour growth compared with *Fsp1*^{KO} tumours (Extended Data Fig. 7g,h), which indicated that human FSP1 can functionally compensate for mouse FSP1 in vivo.

Using this hybrid tumour model, we next tested whether icFSP1 had therapeutic benefit against lung cancer. We found that FSP1 inhibition as a monotherapy improved overall survival of mice bearing lung tumours, almost to the same extent as genetic *Fsp1* deletion (Fig. 5a). To determine whether the therapeutic effect of icFSP1 was indeed due to the induction of ferroptosis, we tested whether LIP1, which we expected to restrict lipid peroxidation induced by FSP1 inhibition, would rescue tumour suppression in icFSP1-treated mice. In correlation with the survival data, we observed that icFSP1 treatment significantly decreased tumour growth compared with vehicle-treated mice, and concomitant LIP1 treatment abrogated the tumour-suppressive effect of icFSP1 treatment (Fig. 5b and Extended Data Fig. 7i). Further, to test whether icFSP1 was exerting an on-target, tumour-specific effect, we repeated the treatment study with an internal control—lung tumours expressing FSP1(Q319K), a mutant that is resistant to icFSP1 but maintains anti-ferroptotic function (Extended Data Fig. 7a,b). We found that icFSP1 treatment specifically extended overall survival of mice bearing tumours expressing wild-type human FSP1 but not those bearing tumours expressing FSP1(Q319K) (Fig. 5c), indicating that indeed the tumour suppression seen with icFSP1 treatment was due to inhibitor activity directly on tumour cells.

We considered whether icFSP1 treatment also affected the tumour microenvironment, but we found no differences in the proportion of total T cells, neutrophils, alveolar or interstitial macrophages between the treatment groups (Extended Data Fig. 7j). These data further suggest that icFSP1 primarily exerts on-target, tumour-specific effects,

although more granular immune profiling is needed to determine the potential effects, and thus potential side effects, of FSP1 inhibition on the tumour microenvironment. Finally, we utilized a patient-derived xenograft (PDX) model (LX465; *KRAS*^{G12D}, *TP53*-mutant) to further assess the therapeutic potential of FSP1 inhibition. We found that icFSP1 treatment significantly decreased PDX tumour growth (Fig. 5d), further bolstering the translational potential of targeting FSP1 in patients with LUAD. These pre-clinical studies with icFSP1 are the first to demonstrate that FSP1 is a promising therapeutic target, and our work highlights FSP1 inhibition as a novel therapeutic strategy for improving disease outcome in patients with lung cancer.

Discussion

Cancer is a disease of hyperproliferation, and cancer cells increase their metabolic output to support sustained growth. This occurs at the cost of increased production of reactive oxygen species that can damage macromolecules such as lipids and have deleterious effects[44,45]. One such effect is excessive lipid peroxidation of membrane-associated PUFA-PLs, which can lead to ferroptosis, a unique non-apoptotic mechanism of cell death. Through our systematic interrogation of the key mechanisms that regulate aberrant lipid peroxidation in vivo, we demonstrated that ferroptosis constitutes a barrier to lung cancer and that lung tumours rely on GPX4 and uniquely, FSP1, to overcome ferroptosis and sustain tumorigenesis (Extended Data Fig. 7k,l).

Our work specifically highlights the dependence of lung tumours on FSP1 in vivo, even in the presence of functional GPX4 (Extended Data Fig. 7k). The companion study by Palma et al.[46] reveals that this dependency extends beyond lung tumours, as they show that metastasizing melanoma cells in the lymph also require FSP1 expression to buffer ferroptosis. These studies are the first reports of a context in which FSP1 and GPX4 are independently required for ferroptosis suppression and therefore either can affect disease outcome. Moreover, analysis of GEMM and human lung tumours demonstrated that FSP1 levels increase during tumour progression and correlate with poor survival. By contrast, GPX4 is ubiquitous in tumours and most tissues. Given that germline *Gpx4*^{KO} mice are not viable[47], whereas *Fsp1*^{KO} mice are viable with no notable physiological defects[20,48,49], the therapeutic window for targeting FSP1 with fewer toxic side effects is expected to be much greater than for GPX4. Furthermore, loss of GPX4 is toxic to T cells, which would suppress any anti-tumour immune responses[50,51]. Leveraging this unique requirement for FSP1 in lung cancer, our studies demonstrate the therapeutic benefit of FSP1 inhibition in promoting ferroptosis, suppressing tumour growth and extending survival as a monotherapy in aggressive pre-clinical lung cancer models. Similarly, the therapeutic potential of FSP1 inhibition in suppressing melanoma lymph node metastases is demonstrated in the accompanying Article[46]. Finally, our studies also underscore the value of in vivo pre-clinical models in capturing physiologically relevant metabolic dependencies that may be missed in vitro and pave the way for development of FSP1 inhibitors for clinical testing in patients with lung cancer.

Online content

Any methods, additional references, Nature Portfolio reporting summaries, source data, extended data, supplementary information, acknowledgements, peer review information; details of author contributions and competing interests; and statements of data and code availability are available at https://doi.org/10.1038/s41586-025-09710-8.

1. Dixon, S. J. et al. Ferroptosis: an iron-dependent form of nonapoptotic cell death. *Cell* **149**, 1060–1072 (2012).
2. Viswanathan, V. S. et al. Dependency of a therapy-resistant state of cancer cells on a lipid peroxidase pathway. *Nature* **547**, 453–457 (2017).
3. Hangauer, M. J. et al. Drug-tolerant persister cancer cells are vulnerable to GPX4 inhibition. *Nature* **551**, 247–250 (2017).
4. Berndt, C. et al. Ferroptosis in health and disease. *Redox Biol* **75**, 103211 (2024).
5. Nakamura, T. & Conrad, M. Exploiting ferroptosis vulnerabilities in cancer. *Nat. Cell Biol.* **26**, 1407–1419 (2024).
6. Friedmann Angeli, J. P. et al. Inactivation of the ferroptosis regulator Gpx4 triggers acute renal failure in mice. *Nat. Cell Biol.* **16**, 1180–1191 (2014).
7. Yang, W. S. et al. Regulation of ferroptotic cancer cell death by GPX4. *Cell* **156**, 317–331 (2014).
8. Bersuker, K. et al. The CoQ oxidoreductase FSP1 acts parallel to GPX4 to inhibit ferroptosis. *Nature* **575**, 688–692 (2019).
9. Doll, S. et al. FSP1 is a glutathione-independent ferroptosis suppressor. *Nature* **575**, 693–698 (2019).
10. Wiernicki, B. et al. Excessive phospholipid peroxidation distinguishes ferroptosis from other cell death modes including pyroptosis. *Cell Death Dis.* **11**, 922 (2020).
11. Conrad, M. & Pratt, D. A. The chemical basis of ferroptosis. *Nat. Chem. Biol.* **15**, 1137–1147 (2019).
12. Dixon, S. J. & Olzmann, J. A. The cell biology of ferroptosis. *Nat. Rev. Mol. Cell Biol.* **25**, 424–442 (2024).
13. Kraft, V. A. N. et al. GTP cyclohydrolase 1/tetrahydrobiopterin counteract ferroptosis through lipid remodeling. *ACS Cent. Sci.* **6**, 41–53 (2020).
14. Soula, M. et al. Metabolic determinants of cancer cell sensitivity to canonical ferroptosis inducers. *Nat. Chem. Biol.* **16**, 1351–1360 (2020).
15. Garcia-Bermudez, J. et al. Squalene accumulation in cholesterol auxotrophic lymphomas prevents oxidative cell death. *Nature* **567**, 118–122 (2019).
16. Qiu, B. et al. Phospholipids with two polyunsaturated fatty acyl tails promote ferroptosis. *Cell* **187**, 1177–1190.e1118 (2024).
17. Kagan, V. E. et al. Oxidized arachidonic and adrenic PEs navigate cells to ferroptosis. *Nat. Chem. Biol.* **13**, 81–90 (2017).
18. Doll, S. et al. ACSL4 dictates ferroptosis sensitivity by shaping cellular lipid composition. *Nat. Chem. Biol.* **13**, 91–98 (2017).
19. Dixon, S. J. et al. Human haploid cell genetics reveals roles for lipid metabolism genes in nonapoptotic cell death. *ACS Chem. Biol.* **10**, 1604–1609 (2015).
20. Mishima, E. et al. A non-canonical vitamin K cycle is a potent ferroptosis suppressor. *Nature* **608**, 778–783 (2022).
21. Seiler, A. et al. Glutathione peroxidase 4 senses and translates oxidative stress into 12/15-lipoxygenase dependent- and AIF-mediated cell death. *Cell Metab.* **8**, 237–248 (2008).
22. Zilka, O. et al. On the mechanism of cytoprotection by ferrostatin-1 and liproxstatin-1 and the role of lipid peroxidation in ferroptotic cell death. *ACS Cent. Sci.* **3**, 232–243 (2017).
23. Jiang, X., Stockwell, B. R. & Conrad, M. Ferroptosis: mechanisms, biology and role in disease. *Nat. Rev. Mol. Cell Biol.* **22**, 266–282 (2021).
24. Nakamura, T. et al. Phase separation of FSP1 promotes ferroptosis. *Nature* **619**, 371–377 (2023).
25. Eaton, J. K. et al. Selective covalent targeting of GPX4 using masked nitrile-oxide electrophiles. *Nat. Chem. Biol.* **16**, 497–506 (2020).
26. Yang, W. S. & Stockwell, B. R. Synthetic lethal screening identifies compounds activating iron-dependent, nonapoptotic cell death in oncogenic-RAS-harboring cancer cells. *Chem. Biol.* **15**, 234–245 (2008).
27. Xavier da Silva, T. N., Schulte, C., Alves, A. N., Maric, H. M. & Friedmann Angeli, J. P. Molecular characterization of AIFM2/FSP1 inhibition by iFSP1-like molecules. *Cell Death Dis.* **14**, 281 (2023).
28. Hendricks, J. M. et al. Identification of structurally diverse FSP1 inhibitors that sensitize cancer cells to ferroptosis. *Cell Chem. Biol.* **30**, 1090–1103.e1097 (2023).
29. Nakamura, T. et al. Integrated chemical and genetic screens unveil FSP1 mechanisms of ferroptosis regulation. *Nat. Struct. Mol. Biol.* **30**, 1806–1815 (2023).
30. Yoshioka, H. et al. Identification of a small molecule that enhances ferroptosis via inhibition of ferroptosis suppressor protein 1 (FSP1). *ACS Chem. Biol.* **17**, 483–491 (2022).
31. Sanchez-Rivera, F. J. et al. Rapid modelling of cooperating genetic events in cancer through somatic genome editing. *Nature* **516**, 428–431 (2014).
32. Ding, H. et al. Activation of the NRF2 antioxidant program sensitizes tumors to G6PD inhibition. *Sci. Adv.* **7**, eabk1023 (2021).
33. Lignitto, L. et al. Nrf2 activation promotes lung cancer metastasis by inhibiting the degradation of Bach1. *Cell* **178**, 316–329.e318 (2019).
34. Romero, R. et al. *Keap1* loss promotes *Kras*-driven lung cancer and results in dependence on glutaminolysis. *Nat. Med.* **23**, 1362–1368 (2017).
35. Best, S. A. et al. Distinct initiating events underpin the immune and metabolic heterogeneity of KRAS-mutant lung adenocarcinoma. *Nat. Commun.* **10**, 4190 (2019).
36. Takahashi, N. et al. 3D culture models with CRISPR screens reveal hyperactive NRF2 as a prerequisite for spheroid formation via regulation of proliferation and ferroptosis. *Mol. Cell* **80**, 828–844.e826 (2020).
37. Zou, Y. et al. A GPX4-dependent cancer cell state underlies the clear-cell morphology and confers sensitivity to ferroptosis. *Nat. Commun.* **10**, 1617 (2019).
38. Vidigal, J. A. & Ventura, A. Rapid and efficient one-step generation of paired gRNA CRISPR–Cas9 libraries. *Nat. Commun.* **6**, 8083 (2015).
39. Ingold, I. et al. Selenium utilization by GPX4 is required to prevent hydroperoxide-induced ferroptosis. *Cell* **172**, 409–422.e421 (2018).
40. Cancer Genome Atlas Research, N. Comprehensive molecular profiling of lung adenocarcinoma. *Nature* **511**, 543–550 (2014).
41. Muller, F. et al. Elevated FSP1 protects KRAS-mutated cells from ferroptosis during tumor initiation. *Cell Death Differ.* **30**, 442–456 (2023).
42. Zavitsanou, A. M. et al. *KEAP1* mutation in lung adenocarcinoma promotes immune evasion and immunotherapy resistance. *Cell Rep.* **42**, 113295 (2023).
43. Koppula, P. et al. A targetable CoQ–FSP1 axis drives ferroptosis- and radiation-resistance in KEAP1 inactive lung cancers. *Nat. Commun.* **13**, 2206 (2022).
44. Wu, K., El Zowalaty, A. E., Sayin, V. I. & Papagiannakopoulos, T. The pleiotropic functions of reactive oxygen species in cancer. *Nat. Cancer* **5**, 384–399 (2024).
45. Cheung, E. C. & Vousden, K. H. The role of ROS in tumour development and progression. *Nat. Rev. Cancer* **22**, 280–297 (2022).

46. Palma, M. et al. Lymph node environment drives FSP1 targetability in metastasizing melanoma. *Nature* https://doi.org/10.1038/s41586-025-09709-1 (2025).
47. Yant, L. J. et al. The selenoprotein GPX4 is essential for mouse development and protects from radiation and oxidative damage insults. *Free Radic. Biol. Med.* **34**, 496–502 (2003).
48. Mei, J., Webb, S., Zhang, B. & Shu, H. B. The p53-inducible apoptotic protein AMID is not required for normal development and tumor suppression. *Oncogene* **25**, 849–856 (2006).
49. Nguyen, H. P. et al. Aifm2, a NADH oxidase, supports robust glycolysis and is required for cold- and diet-induced thermogenesis. *Mol. Cell* **77**, 600–617.e604 (2020).
50. Drijvers, J. M. et al. Pharmacologic screening identifies metabolic vulnerabilities of $CD8^+$ T cells. *Cancer Immunol. Res.* **9**, 184–199 (2021).
51. Matsushita, M. et al. T cell lipid peroxidation induces ferroptosis and prevents immunity to infection. *J. Exp. Med.* **212**, 555–568 (2015).

Methods

Cell lines

KP LUAD cell lines were obtained from the laboratory of T. Jacks. KP, *Fsp1*^{KO} cell lines were generated by transient transfection of PX458 (Addgene #48138) expressing an sgRNA targeting *Fsp1*. Single GFP-positive clones were selected and FSP1 loss was validated by western blot. The 16645 cell line was developed from *Kras*^{G12D} *Stk11*$^{-/-}$ GEMM as previously described[52]. KPC7 cells were obtained from the laboratory of D. Simeone. All cell lines were maintained in DMEM or RPMI 160 (Corning) supplemented with 10% FBS (Sigma Aldrich) and gentamicin (Invitrogen) and were tested for mycoplasma regularly (PlasmoTest, InvivoGen). All mouse cell lines were authenticated by PCR genotyping. All human cell lines used were purchased from ATCC and were authenticated by short-tandem-repeat profiling. Genetic manipulation of cell lines was performed via lentiviral transduction of plasmids, detailed in next section, followed by either puromycin (7 μg ml^{-1}) or hygromycin (800 μg ml^{-1}) selection for 1 week.

Cloning/lentivirus generation

CRISPR–Cas9-mediated knockout of target genes was achieved by cloning sgRNAs into pLenti-USEC or lentiCRISPRv2-puro vectors, as previously described[31]. In short, backbones were digested with Esp3I (New England Biosciences) and purified with a gel extraction kit (QIAGEN). sgRNAs were designed using CRISPick (Broad Institute), obtained from Integrated DNA Technologies (Coralville), annealed, phosphorylated, Esp3I-digested, and ligated into the purified digested backbones using Quick Ligase (New England Biosciences). Double sgRNA ultramers were designed and generated as previously described[38]. In brief, ultramers were Gibson-assembled to digested pDonor_sU6 (Addgene #69351), Esp3I-digested, and ligated to purified digested backbones. Guide RNA sequences used to make gene knockouts can be found in Supplementary Data 4. GPX4, mouse FSP1 and human FSP1 expression plasmids were generated using Gibson assembly of the respective cDNA into pLenti-v2-filler.

Lentivirus was generated by co-transfection of HEK293 cells with a viral vector and packaging plasmids psPAX2 (Addgene #12260) and pMD2.G (Addgene #12259) using PEI transfection reagent. Cell supernatant containing lentivirus was collected 72 h after transfection and filtered through 0.45-μm PVDF filters. For in vivo experiments, lentivirus was concentrated by ultracentrifugation at 25,000 rpm for 2 h at 4 °C. The viral pellet was resuspended in PBS and stored at −80 °C until use. Viral titre was quantified with the use of a Cre-dependent GreenGo reporter cell line. For in vitro experiments, medium containing virus was collected, filtered, and added directly to recipient cells with polybrene at 8 μg ml^{-1} for 48 h before selection.

Mouse models

All mouse experiments described in this study were approved by the NYU Institutional Animal Care and Use Committee (IACUC). Mice were housed according to IACUC guidelines in ventilated caging in a specific pathogen-free animal facility. For all mouse studies, ≥4 mice were used for each experimental condition. *Kras*$^{LSL\text{-}G12D/+}$; *Tp53*$^{fl/fl}$; *Rosa26*$^{LSL\text{-}Cas9/LSL\text{-}Cas9}$ (KPC GEMMs) mice were bred as previously described[31–35]. C57BL/6 J (JAX strain 000664) mice with the appropriate genotype, aged 8 to 12 weeks were randomly selected to begin tumour initiation studies with pUSEC lentivirus. Care was taken to ensure each experimental arm had an equal number of male and female mice. Mice were intratracheally infected with lentiviruses as described and monitored until experimental endpoint. Tumour burden was quantified by H&E staining and analysed using QuPath software as a measurement of total tumour area/total lung lobe area. All quantifications were done with investigator blinded to the respective sample genotypes.

All transplantation experiments were performed using nude (JAX strain 002019), NOD SCID Gamma (NSG; JAX strain 005557 F), C57BL/6 J *Fsp1*-knockout (Conrad group[16]) or C57BL/6 J wild-type (JAX strain mice aged 8 to 12 weeks old). For mouse cell xenograft experiments, 100,000 cells in 100 μl of phosphate-buffered saline (PBS) was injected subcutaneously into each flank of the mouse. For the xenograft studies in Fig. 3 the number of cells injected per flank and whether they were injected with 50:50 PBS and Matrigel (Corning) are indicated as follows: H2009 (2 million cells + Matrigel), H1299 (1 million cells), PC9 (1 million cells), H1975 (2 million cells + Matrigel), A549 (1 million cells), 16645 (500,000 cells), KPC7 (250,000 cells). All human cell line xenograft experiments were carried out in male NSG mice unless specified. For the PDX experiment, tumours were implanted subcutaneously in male NSG mice as previously described[34]. Tumours were measured with callipers, and volume was calculated based on 0.5 × length × width^2. The maximum tumour diameter permitted by our IACUC protocol was 2 cm, and this was not exceeded in any experiment. For orthotopic lung tumour experiments, 100,000 luciferase-expressing cells in 200 μl of PBS were injected intravenously into tail vein of male mice unless specified in the legend. Tumour growth was measured by bioluminescence (PerkinElmer IVIS Spectrum In Vivo Imaging System; D-luciferin, PerkinElmer 122799). Data were analysed using Living Image software.

Antioxidant and drug treatments

For LIP1 treatment, mice were dosed with 10 mg kg^{-1} LIP1 (BOC Sciences) or vehicle (2% DMSO + 40% PEG300 + 2% Tween 80 in sterile H_2O) by intraperitoneal injection for frequency and duration indicated in figure schematics. For icFSP1 treatment, mice were dosed with 50 mg kg^{-1} icFSP1 (WuXi LabNetwork) or vehicle (45% PEG300 in sterile PBS) by intraperitoneal injection twice daily. High (TD.2108412) and low (TD.210841) irradiated vitamin E diets were obtained from Inotivco and provided ad libitum for length of time indicated in figure legends. In all experiments, mice were randomly assigned to treatment group.

Cell clonogenic and viability assays

Cell clonogenic assays were conducted by seeding 2,000 cells per well into 12-well dishes (BD/Falcon) in RPMI-1640 medium. After 12–16 h, medium containing RSL3 and/or LIP1 was added to wells. After 5 days of growth, plates were washed twice with PBS and stained with 0.5% crystal violet (Fisher Scientific) solution in 20% methanol. Plates were dried, scanned, and crystal violet was quantified by solubilization with 10% acetic acid and measurement of absorbance at 592 nm by spectrometer (Molecular Devices). Cell viability assays were conducted by seeding 2,000 cells per well into white-walled, clear-bottom, 96-well plates (Corning) in RPMI-1640 medium. After 12–16 h, medium containing RSL3, LIP1 and/or FSEN1, iFSP1 or icFSP1 was added. After three days, cell viability was assessed by CellTiter-Glo (Promega) and luminescence was measured by spectrometer (Molecular Devices).

Immunoblotting

Cells were plated to 75% confluency in a 6-well dish, and the following day cells were lysed on ice with Pierce RIPA buffer (ThermoScientific) containing 1× protease/phosphatase inhibitor cocktail (Thermo Fisher Scientific). Samples were sonicated in cooled 4 °C water (12 rounds, 30 s on and 30 s off) and then centrifuged at 14,000 rpm at 4 °C for 15 min. The supernatant was collected, and protein was quantified using the DC Rad Protein Assay kit. Protein was diluted to 1 μg μl^{-1} with water and 4× NuPage LDS sample buffer, then boiled at 95 °C for 10 min. Twenty micrograms of protein per well was loaded into Invitrogen 4–12% Bis-Tris gels and then transferred onto PVDF membranes using a standard protocol. PVDF membranes were then blocked using 5% BSA in TBST for 60 min at room temperature and incubated

with primary antibodies in 5% BSA overnight at 4 °C. Primary antibodies were obtained as follows: GPX4 (Abcam), FSP1 (Proteintech), ACSL4 (Santa Cruz Biotechnologies), phospho-ERK (Cell Signaling), ERK (Cell Signaling) and Hsp90 (BD Bioscences). The following day, membranes were washed in TBST and incubated with horseradish peroxidase (HRP)-conjugated secondary antibodies for 1 h at room temperature. Enhanced chemiluminescent horseradish peroxidase substrate (ThermoScientific SuperSignal West PICO Plus) was added to the membrane for 1 min, and the resulting membrane was imaged using the General Electric Amersham Imager 680. For gel source data, see Supplementary Data 1.

Oxidized lipidomics

For the *Gpx4*-knockout experiment, cells were plated to 75% confluency in 6-well dishes. The following day, cells were treated with DMSO, RSL3 (0.5 μM), or RSL3(0.5 μM) plus LIP1(100 nM). After 8 h, cells were collected and washed in an antioxidant solution (PBS containing dibutylhydroxytoluene (100 μM) and diethylenetriamine pentaacetate (100 μM)) and centrifuged. Supernatent was discarded and cell pellets were immediately frozen in liquid nitrogen and stored at −80 °C. Frozen samples were sent on dry ice to Wayne State Lipidomics Core for metabolite extraction and LC–MS analysis.

Fsp1 wild-type and knockout tumour and cell lipidomic analysis were performed in the laboratory of Y.P.K. *Fsp1* wild-type and knockout cells were plated at 75% confluency in 10 cm plates and treated as stated above. After euthanasia, mice were perfused with the antioxidant solution (+3.8% trisodium citrate), orthotopic tumours were microdissected, frozen in liquid nitrogen and stored at −80 °C. Mouse lung cancer tissues were cryopulverized and extracted with chloroform:methanol (2:1, v/v) at a tissue concentration of 25 mg mL^{-1}. For the cells, 1.0×10^7 cells were extracted by 1 ml of chloroform:methanol (2:1, v/v). EquiSPLASH LIPIDOMIX internal standard (Avanti Polar Lipids) was added to the extraction solvent at 0.1 μg ml^{-1} per lipid class. Samples were sonicated on ice for 1 min using a VCX 130 probe sonicator (5 s on/off cycles), incubated for 30 min, and centrifuged at 17,000 × g for 20 min at 4 °C. The supernatant was was dried under vacuum (EZ-2 Elite, Genevac), reconstituted in 10% of the original volume with isopropanol, and transferred to glass autosampler vials for LC–MS analysis. Chromatographic separation was performed using a Waters ACQUITY UPLC CSH C18 column (100 × 2.1 mm, 1.7 μm) with a VanGuard precolumn (5 × 2.1 mm, 1.7 μm). Mobile phase A consisted of acetonitrile/water (60:40, v/v), and mobile phase B of isopropanol/acetonitrile (90:10, v/v), both containing 5 mM ammonium formate and 0.1% formic acid. The column was maintained at 65 °C with a flow rate of 0.6 ml min^{-1}. The gradient was as follows: 0–2 min, 15–30% B; 2–2.5 min, 30–48% B; 2.5–11 min, 48–82% B; 11–11.5 min, 82–99% B; 11.5–12 min, 99% B; 12–12.1 min, 99–15% B; and 12.1–16 min, hold at 15% B for re-equilibration. Mass spectrometry was performed on a Q Exactive Plus Quadrupole-Orbitrap (Thermo Fisher Scientific) equipped with a heated electrospray ionization (HESI) source and operated in negative ion mode. Source settings were: sheath gas, 60 a.u.; auxiliary gas, 25 a.u.; sweep gas, 2 a.u.; spray voltage, 3.0 kV; capillary temperature, 320 °C; S-lens RF level, 50%; and auxiliary gas heater temperature, 370 °C. Parallel reaction monitoring (PRM) was carried out with the following parameters: resolution, 17,500 at m/z 200; AGC target, 2×10^5; maximum injection time, 50 ms; isolation window, m/z 1.2; and stepped normalized collision energies of 20, 30, and 40. The oxidized lipid analysis was adapted by previous PRM based analysis[53]. To generate the PRM inclusion list, pooled sample extracts were first analysed in DDA mode to identify the most abundant polyunsaturated phosphatidylcholine and phosphatidylethanolamine species using Lipostar2[54]. These precursors were subjected to in silico oxidation using LPPtiger2 to predict candidate oxidized lipids. A semi-targeted DDA experiment was then conducted to confirm precursor detectability and finalize the inclusion list[53]. Data were analysed using Skyline (v24.1)[55]. Quantification was based on fragment anions derived from oxidized fatty acyl chains, with peak areas normalized to phosphatidylcholine(15:0/18:1(d7)) or phosphatidylethanolamine(15:0/18:1(d7)) internal standards from the EquiSPLASH LIPIDOMIX mixture.

CoQ_9 and CoQ_9H_2 analysis

CoQ_9 and CoQ_9H_2 analysis was conducted by modification of previous study[56]. The D_9-CoQ_{10} standard was purchased from IsoSciences (Ambler, PA, USA). The D_6-$CoQ_{10}H_2$ standard was synthesized from D_6-CoQ_{10}, which was obtained from Good Laboratory Practice Bioscience (Montclair, CA, USA). The CoQ_9 standard was purchased from Tokyo Chemical Industry (Tokyo, Japan), and CoQ_9H_2 was synthesized from CoQ_9. D_6-$CoQ_{10}H_2$ and D_9-CoQ_{10} were used as internal standards for the CoQ_9H_2 and CoQ_9, respectively. Chloroform: methanol (2:1, v/v), containing internal standards of 0.5 μM of D_6-$CoQ_{10}H_2$ and D_6-CoQ_{10} was used to extract mouse lung cancer tissue at a tissue concentration of 25 mg ml^{-1}. For the cells, 1.0×10^7 cells were extracted by 1 ml of same extraction solvent. Samples were then sonicated on ice for 1 min using a VCX 130 probe sonicator (5 s on/off cycles), incubated for 30 min, and centrifuged at 17,000*g* for 20 min at 4 °C. A 100 μl aliquot of the supernatant was transferred to glass autosampler vials for LC–MS/MS analysis. The liquid chromatography conditions were identical to those used for oxidized lipid analysis. Q Exactive Plus MS was operated in positive ion mode. Source settings were as follows: sheath gas, 60 a.u. (arbitrary units); auxiliary gas, 25 a.u.; sweep gas, 2 a.u.; spray voltage, 3.0 kV; capillary temperature, 320 °C; S-lens RF level, 50%; and auxiliary gas heater temperature, 370 °C. The mass range was *m/z* 120–1,200; resolution, 70,000 at *m/z* 200; AGC target, 1×10^6; and maximum injection time, 100 ms. By using EL–MAVEN (v0.12.0), the LC–MS peaks of CoQ_9, CoQ_9H_2, D_6-$CoQ_{10}H_2$, D_6-CoQ_{10}, and D_9-CoQ_{10} were identified by matching with standard library and their peak areas were extracted with 10 ppm error range. Standard curves were generated using known concentrations of CoQ_9H_2 and CoQ_9, and used to calculate the concentrations of CoQ_9H_2 and CoQ_9 in the samples following an algorithm described in a previous study[56].

Immunohistochemistry

Tumour-bearing mice were euthanized by carbon dioxide asphyxiation, after which the lungs were dissected and fixed in 4% PFA solution overnight. Fixed lungs were washed with PBS 2 times, transferred, and stored in 70% ethanol, until cassette loading and paraffin embedding. Sections were cut and stained with H&E. For immunohistochemistry with the exception of TUNEL staining, sections were immunostained on a Leica BondRX automated stainer according to the manufacturer's instructions. In brief, tissues underwent deparaffinization online, followed by epitope retrieval for 20 min at 100° with Leica Biosystems ER2 solution (pH9, AR9640), endogenous peroxidase activity blocking with H_2O_2, and non-specific binding site blocking with Rodent Block M (Biocare, RBM961L) and Bond Primary Antibody Diluent (Leica Biosystems, AR9352). Sections were then incubated with primary antibodies against GPX4 (Abcam), FSP1 (obtained from M. Conrad), 4-HNE (JaICA), Ki67 and cleaved caspase-3 for 60 min at room temperature. Primary antibodies were detected with anti-rat HRP-conjugated polymer (Biocare, BRR4016H), 3,3′-diaminobenzidine (DAB) substrate (provided in the Leica BOND Polymer Refine Detection System, DS9800), and for 4-HNE staining Bond DAB Enhancer (Leica Biosystems, AR9432). Following counter-staining with haematoxylin, slides were scanned at 40× on a Hamamatzu Nanozoomer (2.0HT). TUNEL staining was performed by Histowiz according to their protocol.

For OPAL imaging, coronal 5-μm sections were immunostained on a Leica BondRx auto-stainer according to the manufacturer's instructions. In brief, sections were deparaffiinized online and then treated with 3% H_2O_2 to inhibit endogenous peroxidases, followed by antigen

retrieval with either ER1 (Leica, AR9961; pH6) or ER2 (Leica, AR9640; pH9) retrieval buffer at 100 °C for 20 min. After blocking with either Rodent Block M (Biocare, RBM961L) or Primary Antibody Diluent (Leica, AR93520), slides were incubated with the first primary antibody (FSP1 (obtained from M. Conrad); phospho-ERK1/2, CST; GPX4, Abcam) and secondary HRP polymer pair, followed by HRP-mediated tyramide signal amplification with a specific Opal fluorophore. Once the Opal fluorophore was covalently linked to the antigen, primary and secondary antibodies were removed with a heat retrieval step. This sequence was repeated three more times with subsequent primary and secondary antibody pairs, using a different Opal fluorophore with each primary antibody (see table below for primary antibody sequence and reagent details). After antibody staining, sections were counterstained with spectral DAPI (Akoya Biosciences, FP1490) and mounted with ProLong Gold Antifade (ThermoFisher Scientific, P36935). Semi-automated image acquisition was performed on an Akoya Vectra Polaris (PhenoImagerHT) multispectral imaging system. Slides were scanned at 20× magnification using PhenoImagerHT 2.0 software in conjunction with Phenochart 2.0 and InForm 3.0 to generate unmixed whole slide qptiff scans. All image files were uploaded to the NYUGSoM's OMERO Plus image data management system (Glencoe Software).

Flow cytometry

Lung tissue was processed into a single-cell suspension for flow cytometry as previously described[42,57]. In brief, prior to euthanasia, mice were injected with 2 µg of Anti-mouse CD45-APC conjugated antibody (Biolegend, Clone 30-F11, 103111) retro-orbitally. Lungs were harvested and digested with Collagenase (Sigma-Aldrich, C5138) and deoxyribonuclease I (Sigma-Aldrich, DN25) followed by red blood cell lysis. Single cells were then resuspended in fluorescence-activated cell sorting (FACS) buffer and stained using the following antibodies: CD45 (Biolegend, 103132), CD11b (Biolegend, 101216), CD11c (Biolegend, 117324), Ly6G (Biolegend, 127622), MHCII (BD, 748708), CD103 (Biolegend, 121433), CD64 (Biolegend, 139309), SiglecF (BD, 740956), MertK (R&D, BAF591), CD45 (BD, 748371), CD3e (BD, 740854), CD4 (Invitrogen, MCD0428), CD8a (EBioscience, 563152) and Secondary (Streptavidin) (BD, 564176). Samples were run on the BD LSRFortessa and analysed on FlowJo version 10. Gating strategy is presented in Supplementary Data 2.

TCGA analyses

Gene expression profiles of primary tumours and relevant clinical data of 515 patients with LUAD were obtained from The Cancer Genome Atlas6 (TCGute.org). *GPX4* and *FSP1* (*AIFM2*) mutational status of TCGA tumour samples was retrieved from cBioPortal151 using the TCGA PanCancer Atlas collection (https://gdc.cancer.gov/about-data/publications/pancanatlas). For survival data, patients were stratified based on *GPX4* or *FSP1* expression and overall survival rates were plotted to compare patients with high-*GPX4* or *FSP1* expression (top 50% above median expression) with the rest of the cohort (n = 464 patients). All survival analyses were conducted using the survival curve analyses in GraphPad Prism v9.

Statistics and reproducibility

Statistical analysis was performed using GraphPad Prism v9. All data are expressed as mean plus standard error of the mean, unless otherwise specified. Data were analysed by statistical tests as indicated in figure legends. All tests were two-tailed and replicates are biological unless otherwise stated. All western blots were replicated at least three times with results reproducible of data shown in figures. All in vitro assays were replicated at least three times with a minimum of $n = 3$ biological replicates per group for statistical power. For all in vivo experiments, the minimum sample size was four independent mice or tumours and respective sample size per genotype or condition is further specified in the figure legend. Sample size was not calculated but was chosen in each experiment based on previous experience with various models and to ensure that there were enough samples for statistical power. All in vivo experiments were replicated at least twice with results reproducible of data shown in figures. When representative images are shown, a minimum of three samples from the larger cohort were stained from each group. In the case of representative MRI images, all mice from the cohort were imaged. During sample processing and analysis for the lipidomic the samples were given numeric IDs which after analysis, were unblinded and graphed. For histological and immunohistochemistry analysis, researcher was blinded to the sample condition. The investigators were not blinded during most other data collection or analysis.

Reporting summary

Further information on research design is available in the Nature Portfolio Reporting Summary linked to this article.

Data availability

All data and raw gel images are included with the paper. Raw lipidomic data have been deposited in the MassIVE data base (https://massive.ucsd.edu/) under accession number MSV000098883. Analysed lipidomic data are available in Supplementary Data 3. Gene expression profiles of primary tumours and relevant clinical data of 515 patients with LUAD were obtained from The Cancer Genome Atlas (https://www.cancer.gov/ccg/research/genome-sequencing/tcga). *GPX4*, *FSP1* (*AIFM2*), *KRAS*, *EGFR*, *KEAP1* and *STK11* mutational status of TCGA tumour samples was retrieved from cBioPortal151 using the TCGA PanCancer Atlas collection (https://gdc.cancer.gov/about-data/publications/pancanatlas). All other materials are available upon request from T.P. Source data are provided with this paper.

52. Winslow, M. M. et al. Suppression of lung adenocarcinoma progression by Nkx2-1. *Nature* **473**, 101–104 (2011).
53. Criscuolo, A. et al. Analytical and computational workflow for in-depth analysis of oxidized complex lipids in blood plasma. *Nat. Commun.* **13**, 6547 (2022).
54. Goracci, L. et al. Lipostar, a comprehensive platform-neutral cheminformatics tool for lipidomics. *Anal. Chem.* **89**, 6257–6264 (2017).
55. Adams, K. J. et al. Skyline for small molecules: a unifying software package for quantitative metabolomics. *J. Proteome Res.* **19**, 1447–1458 (2020).
56. Kang, Y. P., Kim, T. H., Ngoc Nguyen, C. T., Kim, S. M. & Kwon, S. W. Robust determination of coenzyme Q10 redox status using two isotope-labeled internal standards. Preprint at https://doi.org/10.2139/ssrn.4982487 (2024).
57. Pillai, R. et al. Glutamine antagonist DRP-104 suppresses tumor growth and enhances response to checkpoint blockade in KEAP1 mutant lung cancer. *Sci. Adv.* **10**, eadm9859 (2024).

Acknowledgements We thankG. Ward and C. Loomis from the Experimental Pathology Core (RRID:SCR_017928) at NYU Langone Health, which is partially supported by the Cancer Center Support Grant P30CA016087 at NYU Langone's Laura and Isaac Perlmutter Cancer Center, for support with immunohistochemistry staining and imaging. The PhenoImagerHT Mutlispectral imaging system was initially purchased through a Shared Instrumentation Grant S10OD021747. We thank the Wayne State University School of Medicine Lipidomics Core Facility, which is supported in part by National Center for Research Resources, National Institutes of Health Grants S10RR027926 and S10OD032292, for support with LC–MS. The analysis of FSP1-oxidized lipids and CoQ_9 were conducted by the Proteomics and Metabolomics Core at the College of Pharmacy, Seoul National University, South Korea. We thank R. Possemato and S. Kotschi for critical reading of this manuscript. We acknowledge J. Teixeira for supporting and motivating this work. T.P. is supported by NIH grants (R37CA222504, R01CA227649, R01CA283049 and R01CA262562) and an American Cancer Society Research Scholar Grant (RSG-17-20001–TBE). K.W. is supported by the Ruth L. Kirschstein Individual Predoctoral NRSA fellowship (F30CA275258) and NIH training grants (T32GM136573 and T32GM136542). A.J.V. is supported by the NIH training grant (T32GM136542). M.C. received funding from the Deutsche Forschungsgemeinschaft (DFG) (CO 291/7-1), the Priority Program SPP 2306 (CO 291/9-1, 461385412 and CO 291/10-1, 461507177) and the European Research Council (ERC) under the European Union's Horizon 2020 research and innovation program (grant agreement GA 884754).

Author contributions T.P., K.W. and A.J.V. designed and directed the study. K.W., A.J.V., J.P.B., A.Z., M.N.N., and M.M. performed various in vitro and in vivo experiments reported in the study. R.P. performed FACS for lung tumour immune profiling. Y.H. performed TCGA patient data analyses. S.M.K. performed FSP1 epilipidomics and CoQ measurements, T.H.K. assisted with data analysis, and Y.P.K. supervised. L.W. and D. Simeone provided guidance for the pancreatic cancer experiment. S.C. performed unbiased tumour burden quantification. M.M. and S.R.

maintained and genotyped all experimental mice. M.C., T.N., M.H. and D. Shackelford provided conceptual advice. T.P., K.W. and A.J.V. wrote the manuscript with comments and input from all authors.

Competing interests T.P. received funding from Pfizer Medical Education Group, Dracen Pharmaceuticals, Kymera Therapeutics, Bristol Myers Squibb and Agios Pharmaceuticals not related to the submitted work. M.C. is a co-founder and shareholder of ROSCUE Therapeutics GmbH. M.C. and T.N. have filed a patent application (WO2024115673A1) for some of the FSP1 inhibitor compounds described here. The other authors declare no competing interests.

Additional information

Supplementary information The online version contains supplementary material available at https://doi.org/10.1038/s41586-025-09710-8.

Correspondence and requests for materials should be addressed to Thales Papagiannakopoulos.

Peer review information *Nature* thanks Jiyeon Kim, Hozumi Motohashi and the other, anonymous, reviewer(s) for their contribution to the peer review of this work. Peer review reports are available.

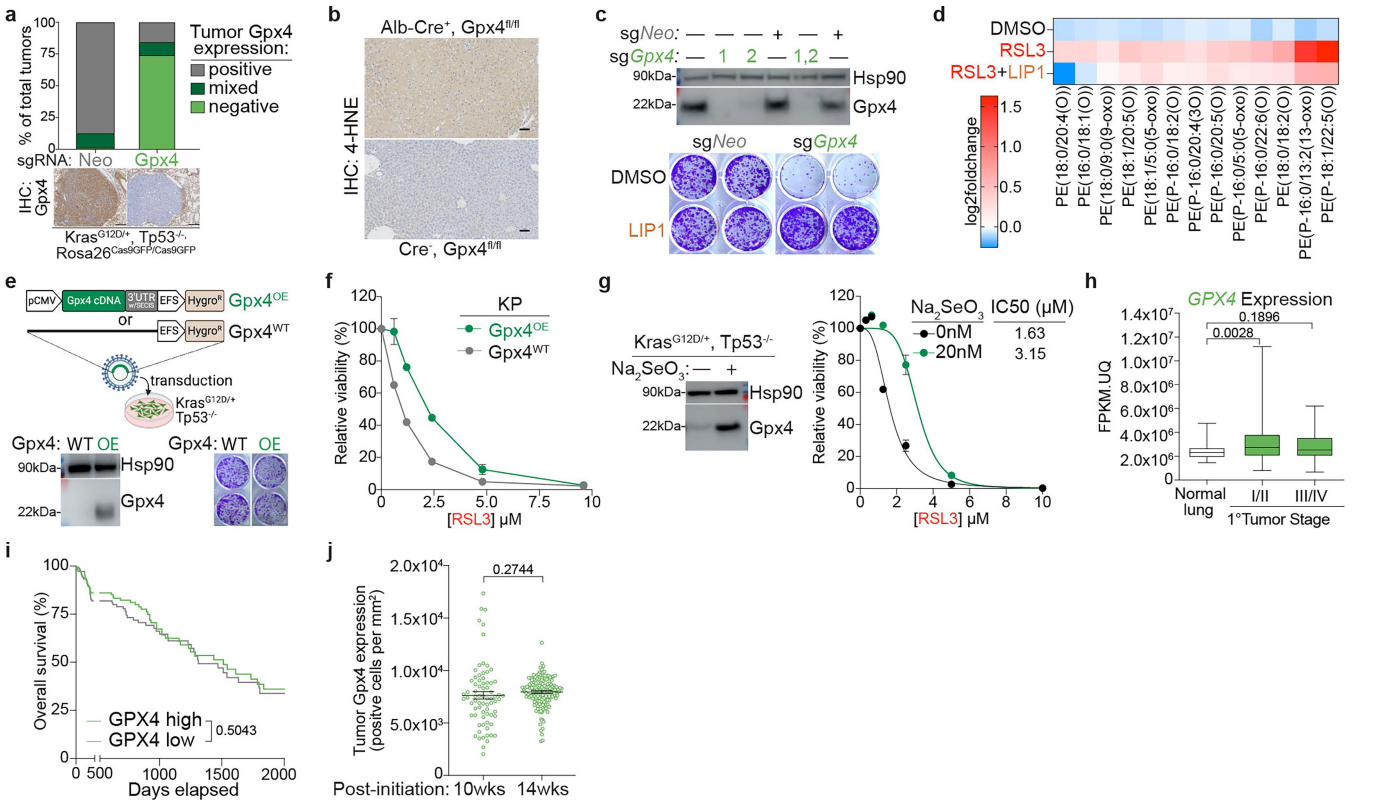

Extended Data Fig. 1 | Gpx4 is required by lung cancer cells. a, Quantification and representative images of Gpx4 IHC in KP LUAD GEMM tumours with knockout of either control (Neo, n = 11) or Gpx4 (n = 12). Scale bars: 200 µm. **b**, Representative 4-hydroxy-2-noneal (4-HNE) IHC of liver tissue from conditional *Gpx4*-knockout mice. Scale bars: 100 µm. **c**, Top: Western blot of KP LUAD cells with CRISPR/Cas9-mediated genetic deletion of Gpx4 with either two individual or duplexed sgRNAs. Bottom: representative images of crystal violet clonogenic assay of KP LUAD cells with knockout of either control (Neo) or Gpx4. Cells were treated with 100 nM LIP1. **d**, Heatmap of LC-MS detection of oxidized phospholipids in KP LUAD cells treated with DMSO control, RSL3 (0.5 µM), and RSL3 (0.5 µM) + LIP1 (100 nM) for 8 h. **e**, Schematic of Gpx4 ectopic overexpression (OE) method in KP LUAD cells. Western blot and representative images of crystal violet clonogenic assay of KP LUAD cells with wildtype (WT) or OE of Gpx4. **f**, CellTiter-Glo Luminescence viability assay of KP, $Gpx4^{WT}$ or $Gpx4^{OE}$ cells upon increasing concentrations of RSL3 (n = 5 per group). **g**, Western blot of KP LUAD cells treated with 20 nM Na_2SeO_3 or DMSO. CellTiter-Glo Luminescence viability assay of KP LUAD cells treated with 20 nM Na_2SeO_3 or DMSO with increasing RSL3 addition (n = 5 per group). **h**, *GPX4* expression in *KRAS*-mutant primary LUAD tumours from TCGA, divided into early and late tumour stages (normal lung, n = 54; stage I/II, n = 354; stage III/IV, n = 98). **i**, Overall survival of *KRAS*-mutant LUAD patients (n = 464) from TCGA, stratified by high vs low tumour *GPX4* expression. **j**, Tumour Gpx4 IHC quantification of KP LUAD GEMM tumours at 10 weeks (n = 4) vs 14 weeks (n = 4) post-tumour initiation. Box plots indicate median (middle line), 25th, 75th percentile (box) and 5th and 95th percentile (whiskers). Data are represented as mean values, error bars represent SEM, significance determined via one-way ANOVA with multiple comparisons (panel **h**), two-sided student's t-test (panel **j**) or Kaplan-Meier simple survival analysis (panel **i**). For gel source data, see Supplementary Data 1. Drawing in **d** created in BioRender. Vaughan, A. (2025) https://BioRender.com/99qhixq.

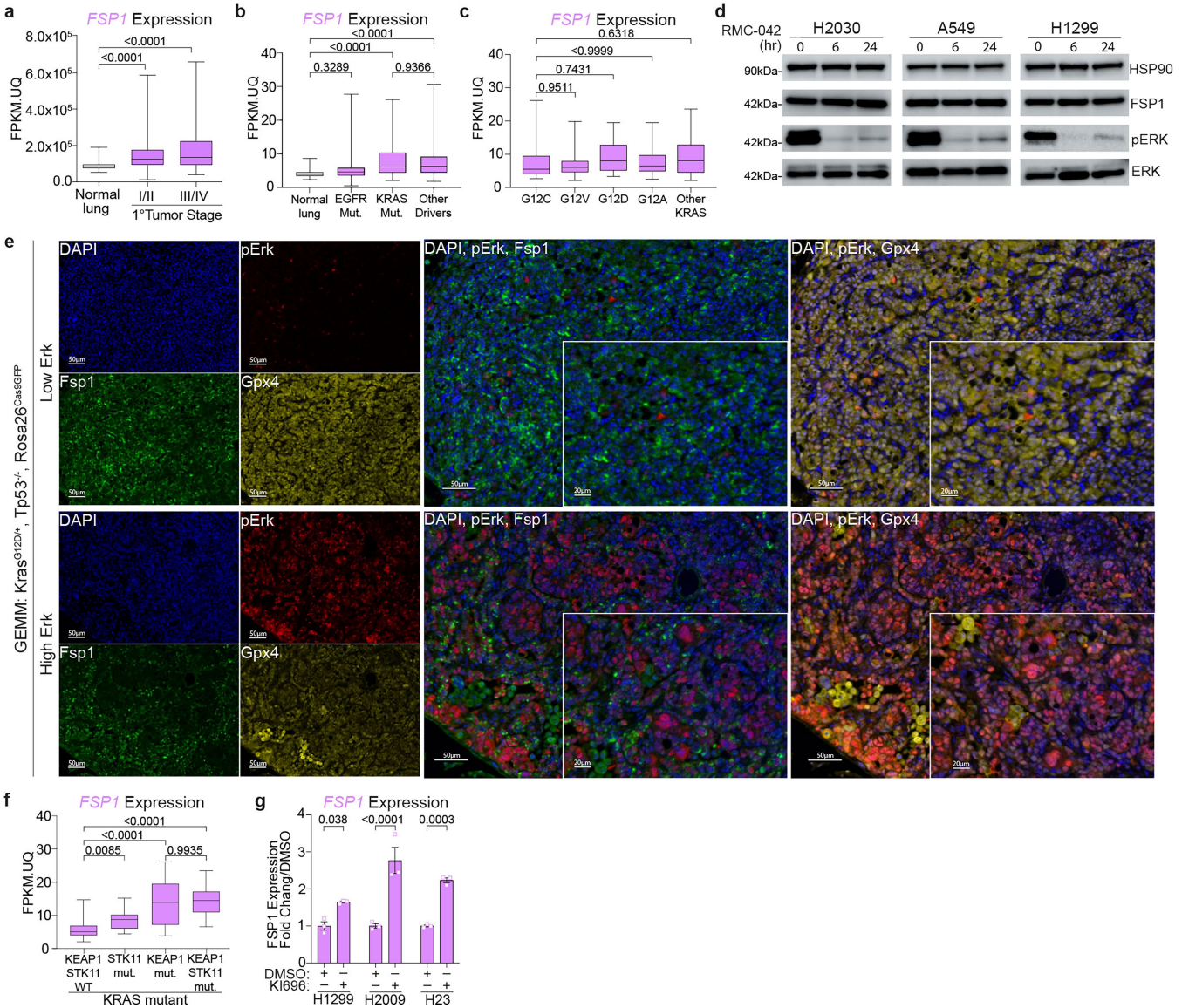

Extended Data Fig. 2 | FSP1's anti-ferroptotic function is not dependent on oncogenic signalling. a, *FSP1* (*AIFM2*) expression of *KRAS*-mutant primary LUAD tumours from TCGA, divided into early and late tumour stages (normal lung, n = 54; stage I/II, n = 354; III/IV, n = 98). **b**, *FSP1* (*AIFM2*) expression of *KRAS*-mutant primary LUAD tumours from TCGA, separated by the *KRAS* mutation (G12C n = 51; G12V n = 32; G12D n = 17; G12A n = 16; other n = 20). **c**, *FSP1* (*AIFM2*) expression of primary LUAD tumours from TCGA, separated by oncogenic driver mutation (normal lung, n = 59; EGFR, n = 71; KRAS, n = 135; other n = 307). **d**, Western blot of KP LUAD human cell lines treated with 50 nM RMC-042 for indicated durations. **e**, representative multi-IF images of KP tumours for markers indicated. Panels are 10X, scale bars: 50 μm; insets are 20X, scale bars: 20 μm. **f**, *FSP1* (*AIFM2*) expression of *KRAS*-mutant primary LUAD tumours from TCGA, separated by tumour co-mutation status (*KEAP1*/*STK11* WT n = 88; *STK11* mutant n = 20; *KEAP1* mutant n = 16; *KEAP1*/*STK11* mutant n = 11). **g**, *FSP1* (*AIFM2*) expression in KP LUAD human cell lines treated with an Nrf2 activator, KI696, for 5 days (n = 3 per group). Box plots indicate median (middle line), 25th, 75th percentile (box) and 5th and 95th percentile (whiskers). Data are represented as mean values, error bars represent SEM, significance determined via one-way ANOVA with multiple comparisons (panels **a**–**c**, **f**, **g**). For gel source data, see Supplementary Data 1.

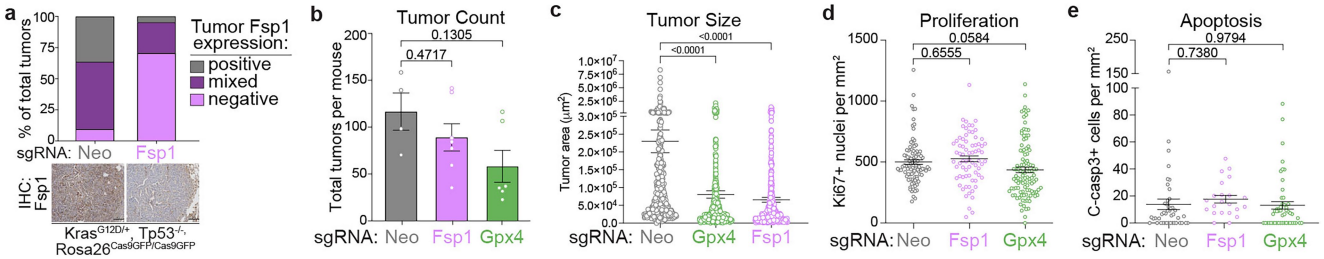

Extended Data Fig. 3 | Neither Fsp1 nor Gpx4 have an impact on tumour initiation, proliferation, or apoptosis. a, Quantification and representative images of tumour Fsp1 IHC in KP LUAD GEMMs with knockout of either control (Neo, n = 11) or Fsp1 (n = 14). Scale bars: 100 µm. **b**, Tumour number quantification in KP LUAD GEMMs with tumour-specific knockout of either control (Neo, n = 4), Fsp1 (n = 7), or Gpx4 (n = 6). **c**, Individual area of KP LUAD GEMM tumours with knockout of either control (Neo, n = 465), Fsp1 (n = 453), or Gpx4 (n = 384). **d**, Quantification of Ki67 IHC of KP LUAD GEMM tumours with knockout of either control (Neo, n = 355), Fsp1 (n = 268), or Gpx4 (n = 291). **e**, Quantification of cleaved caspase-3 IHC of KP LUAD GEMM tumours with knockout of either control (Neo, n = 46), Fsp1 (n = 22), or Gpx4 (n = 52). Data are represented as mean values, error bars represent SEM, significance determined via one-way ANOVA with multiple comparisons (panels **b**–**e**).

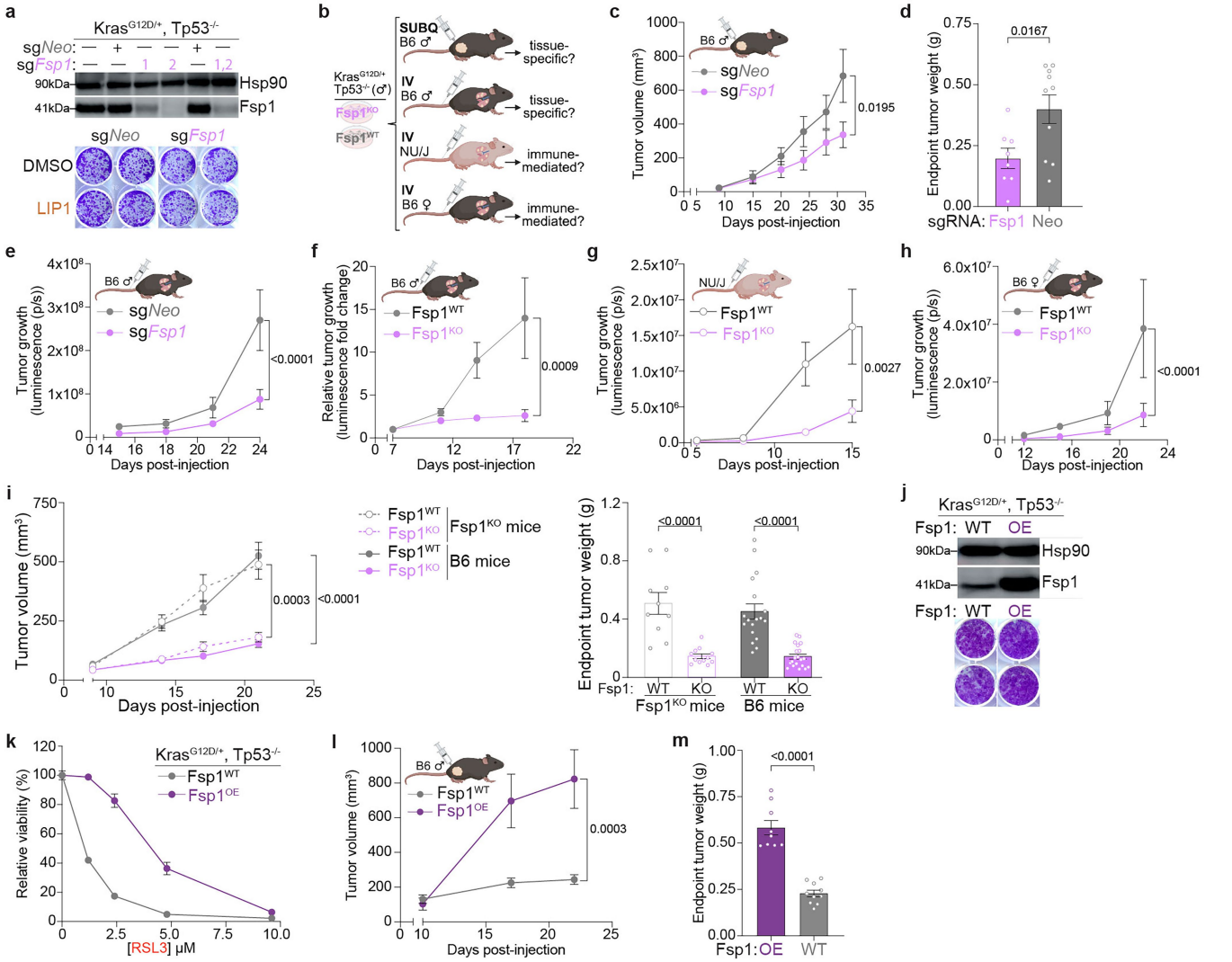

Extended Data Fig. 4 | Fsp1 is required for cell-autonomous tumour growth in vivo. a, Top: Western blot of KP LUAD cells with CRISPR/Cas9-mediated genetic deletion of Fsp1 with either two individual or duplexed sgRNAs. Bottom: representative images of crystal violet clonogenic assay of KP LUAD cells with knockout of either control (Neo) or Fsp1. Cells were treated with 100 nM LIP1. **b**, Schematic depicting all transplantation models performed using isogenic KP, Fsp1^{KO} and Fsp1^{WT}. **c,d**, Longitudinal growth and endpoint tumour weights of KP sg*Fsp1* (n = 8) versus control (sg*Neo* n = 10) subcutaneous (subQ) xenograft tumor transplanted into C57BL/6 J male mice. **e**, Longitudinal lung tumour growth (measured via bioluminescence) in C57BL/6 J male mice orthotopically transplanted with KP LUAD cells with CRISPR/Cas9-mediated knockout of Fsp1 (n = 8) or control (n = 7). **f**, Longitudinal lung tumour growth (measured via bioluminescence normalized to first timepoint (day 7)) in C57BL/6 J male mice orthotopically transplanted with isogenic KP, Fsp1^{KO} (n = 6) and Fsp1^{WT} (n = 7) cells. **g**, Longitudinal lung tumour growth (measured via absolute bioluminescence) in NU/J immunocompromised mice orthotopically transplanted with isogenic KP, Fsp1^{KO} (n = 6) and Fsp1^{WT} (n = 7) cells. **h**, Longitudinal lung tumour growth (measured via absolute bioluminescence) in C57BL/6 J female mice with orthotopic transplantation of isogenic KP, Fsp1^{KO} (n = 8) and Fsp1^{WT} (n = 8) cells. **i**, Longitudinal tumour growth and endpoint tumour weights of either isogenic KP, Fsp1^{KO} or Fsp1^{WT} subcutaneous (subQ) xenograft tumours transplanted in either C57BL/6 J WT (Fsp1^{KO}, male n = 10 female n = 10; Fsp1^{WT}, male n = 8, female n = 10) or C57BL/6 J *Fsp1*-knockout mice (Fsp1^{KO}, males n = 6, females n = 6; Fsp1^{WT}, male n = 4, female n = 6). **j**, Western blot of KP LUAD cells with wildtype (WT) or overexpression (OE) of Fsp1. Representative images of crystal violet clonogenic assay of KP LUAD cells with Fsp1^{WT} or Fsp1^{OE}. **k**, CellTiter-Glo Luminescence viability assay of KP, Fsp1^{WT} or Fsp1^{OE} cells (5 biological replicates per group) with increasing concentrations of RSL3. **l,m**, Longitudinal growth and endpoint weights of KP Fsp1^{WT} (n = 10) or Fsp1^{OE} (n = 10) subcutaneous (subQ) xenograft tumour transplanted into C57BL/6 J male mice. Data are represented as mean values, error bars represent SEM, significance determined via one-way ANOVA with multiple comparisons (panel **i**), two-way ANOVA with Tukey's multiple comparisons test (panels **c**, **e**–**h**, **l**), or two-sided student's t-test (panels **d, m**). For gel source data, see Supplementary Data 1. Drawings in **b**,**c**,**e**–**h**,**l** created in BioRender. Vaughan, A. (2025) https://BioRender.com/99qhixq.

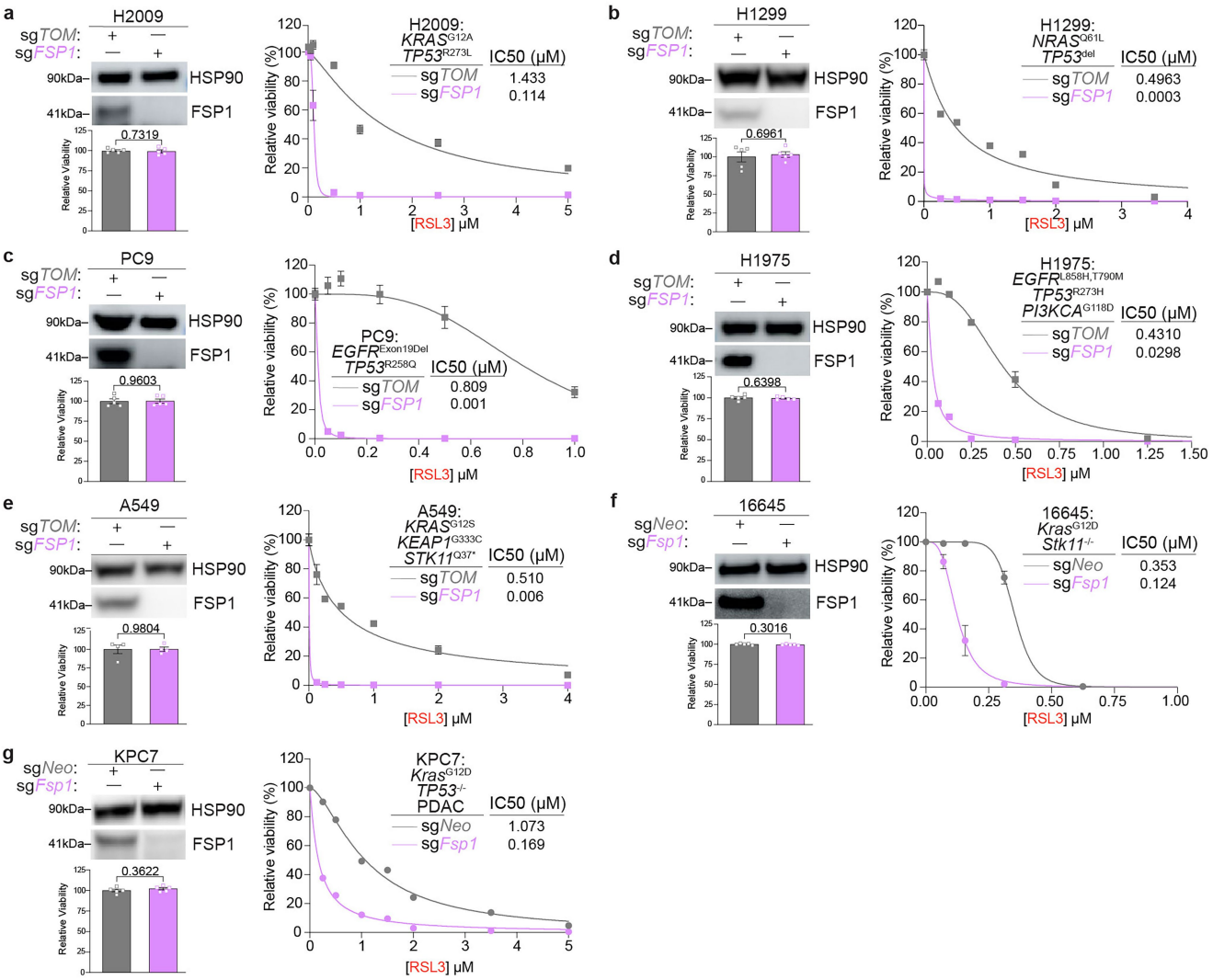

Extended Data Fig. 5 | FSP1 loss in vitro does not induce ferroptosis without RSL3. a, Top: Western blot; bottom: baseline growth (normalized to control); and right: CellTiter-Glo Luminescence viability assay of H2009 cells with the lentiviral addition of Cas9 and guide RNAs targeting FSP1 or a non-targeting control (TOM) (at least 4 biological replicates per group). Viability assay is upon increasing concentrations of RSL3. **b**, As in **a**, but with H1299 cells. **c**, As in **a**, but with PC9 cells. **d**, As in **a**, but with H1975 cells. **e**, As in **a**, but with A549 cells. **f**, As in **a**, but with 16645 cells. **g**, As in **a**, but with KPC7 cells. Data are represented as mean values, error bars represent SEM, significance determined via two-sided student's t-test (panels **a**–**g**). For gel source data, see Supplementary Data 1.

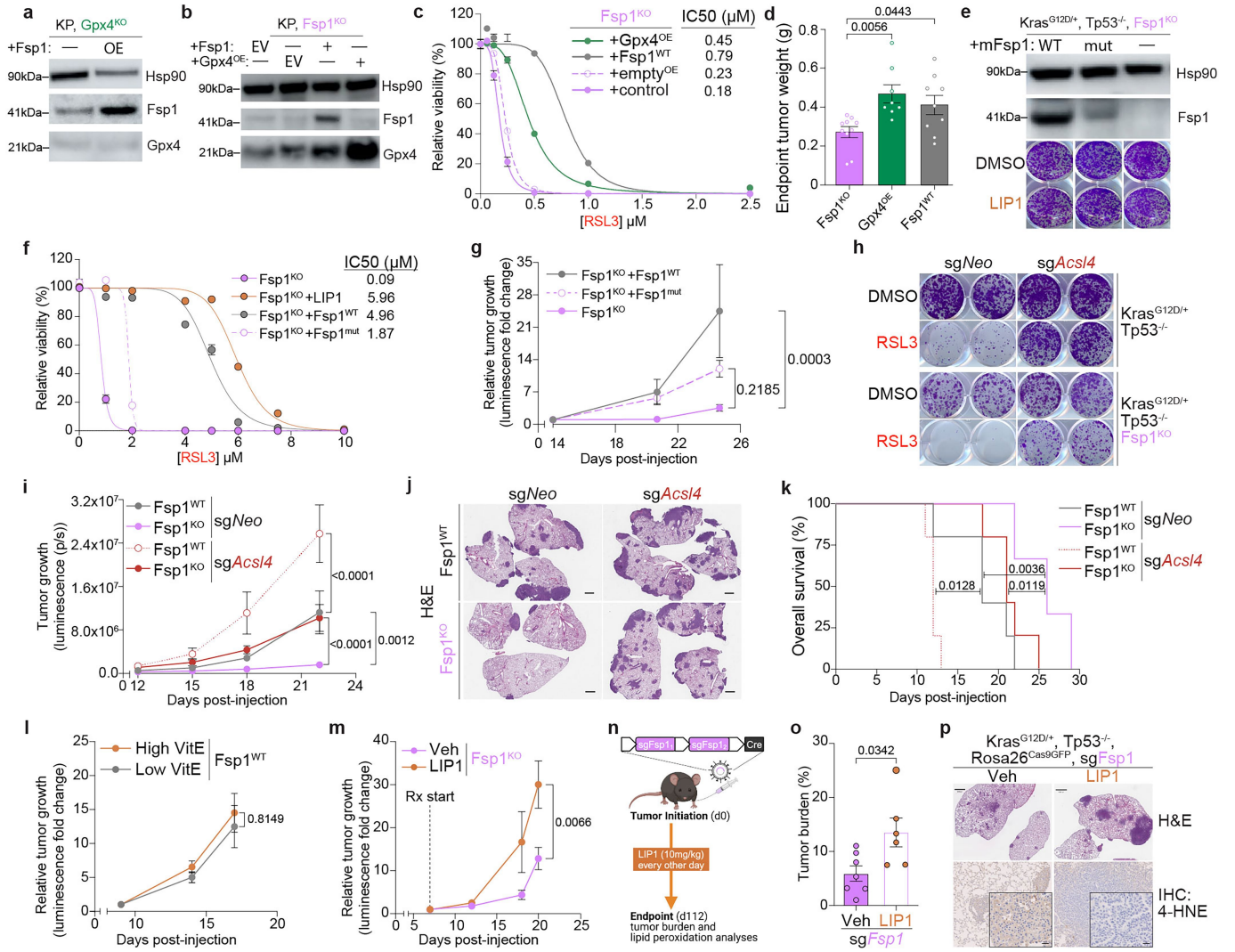

Extended Data Fig. 6 | Fsp1 loss promotes tumour cell ferroptosis. **a**, Western blot of KP, Gpx4^{KO} LUAD cells with either empty vector (–) or Fsp1^{OE}. **b**, Western blot of KP, Fsp1^{KO} LUAD cells with re-expression of either empty vector (–), Fsp1^{WT}, Gpx4^{OE}. **c**, CellTiter-Glo Luminescence viability assay of KP, Fsp1^{KO} LUAD cells in **b** upon increasing concentrations of RSL3. **d**, Endpoint tumour weights of subcutaneous (subQ) xenograft tumours from indicated cell lines transplanted in C57BL/6 J female mice (control n = 10; Fsp1^{WT}, n = 9; Gpx4^{OE}; n = 8). **e**, Top: Western blot of KP, Fsp1^{KO} LUAD cells with re-expression of either empty vector (–), wildtype (WT) Fsp1, or mutant (mut) Fsp1. Bottom: representative images of crystal violet clonogenic assay. **f**, CellTiter-Glo Luminescence viability assay of KP, Fsp1^{KO} LUAD cells with re-expression of either empty vector (Fsp1^{KO}), Fsp1^{WT}, or Fsp1^{mut} upon increasing concentrations of RSL3. LIP1 used at 100 nM. **g**, Longitudinal tumour growth (measured via bioluminescence normalized to initial imaging timepoint (day14)) in C57BL/6 J male mice orthotopically transplanted with isogenic KP, Fsp1^{KO} LUAD cells with re-expression of either empty control vector (Fsp1^{KO}, n = 7), Fsp1^{WT} (n = 7), or Fsp1^{mut} (n = 7). **h**, Representative images of crystal violet clonogenic assay of KP, Fsp1^{WT} or Fsp1^{KO} LUAD cells with CRISPR/Cas9- mediated knockout of control (Neo) or Acsl4. **i**, Longitudinal tumour growth (measured by bioluminescence) of C57BL/6 J male mice with orthotopic transplantation of isogenic KP, Fsp1^{KO} and Fsp1^{WT} cells with CRISPR/Cas9-mediated knockout of control (Neo) or Acsl4 (WT, n = 5; Acsl4^{KO}, n = 4; Fsp1^{KO}, n = 7; Fsp1^{KO}Acsl4^{KO}, n = 7). **j**, Representative H&E of experiment in **i**. Scale bars: 1000 μm. **k**, Overall survival of C57BL/6 J male mice with orthotopic transplantation of isogenic KP, Fsp1^{KO} and Fsp1^{WT} cells with CRISPR/Cas9-mediated knockout of control (Neo) or Acsl4 (n = 5 per group). **l**, Longitudinal tumour growth (measured via bioluminescence normalized to first imaging timepoint (day7)) of C57BL/6 J mice orthotopically transplanted with KP, Fsp1^{WT} cells and receiving high (n = 6) or low (n = 5) VitE diets *ad libitum* 5 days pre-tumor initiation. **m**, Tumour bioluminescence signal normalized to first imaging timepoint (day7) of C57BL/6 J mice orthotopically transplanted with KP, Fsp1^{KO} cells and receiving Liproxstatin-1 (LIP1, n = 7) or vehicle (Veh, n = 5) daily after tumour establishment. **n**, Schematic of KP LUAD GEMMs intratracheally infected with pUSEC lentiviruses containing dual sgRNAs targeting Fsp1. Mice were dosed with LIP1 (n = 6) or Vehicle (Veh, n = 6) every other day starting from tumour initiation. **o**, Tumour burden of KP LUAD GEMMs with CRISPR/Cas9-mediated knockout of Fsp1 and treated with Veh or LIP1. **p**, Representative H&E and 4-HNE IHC of KP LUAD GEMM tumours with knockout of Fsp1 and treated with Veh or LIP1. Scale bars: 1000 μm. Data are represented as mean values, error bars represent SEM, significance determined via one-way ANOVA (panel **d**), two-way ANOVA with Tukey's multiple comparisons (panels **g, i, l, m**), two-sided student's t-test (panel **o**), or Kaplain-Meier simple survival analysis (panel **k**). For gel source data, see Supplementary Data 1. Drawing in **n** created in BioRender. Vaughan, A. (2025) https://BioRender.com/99qhixq.

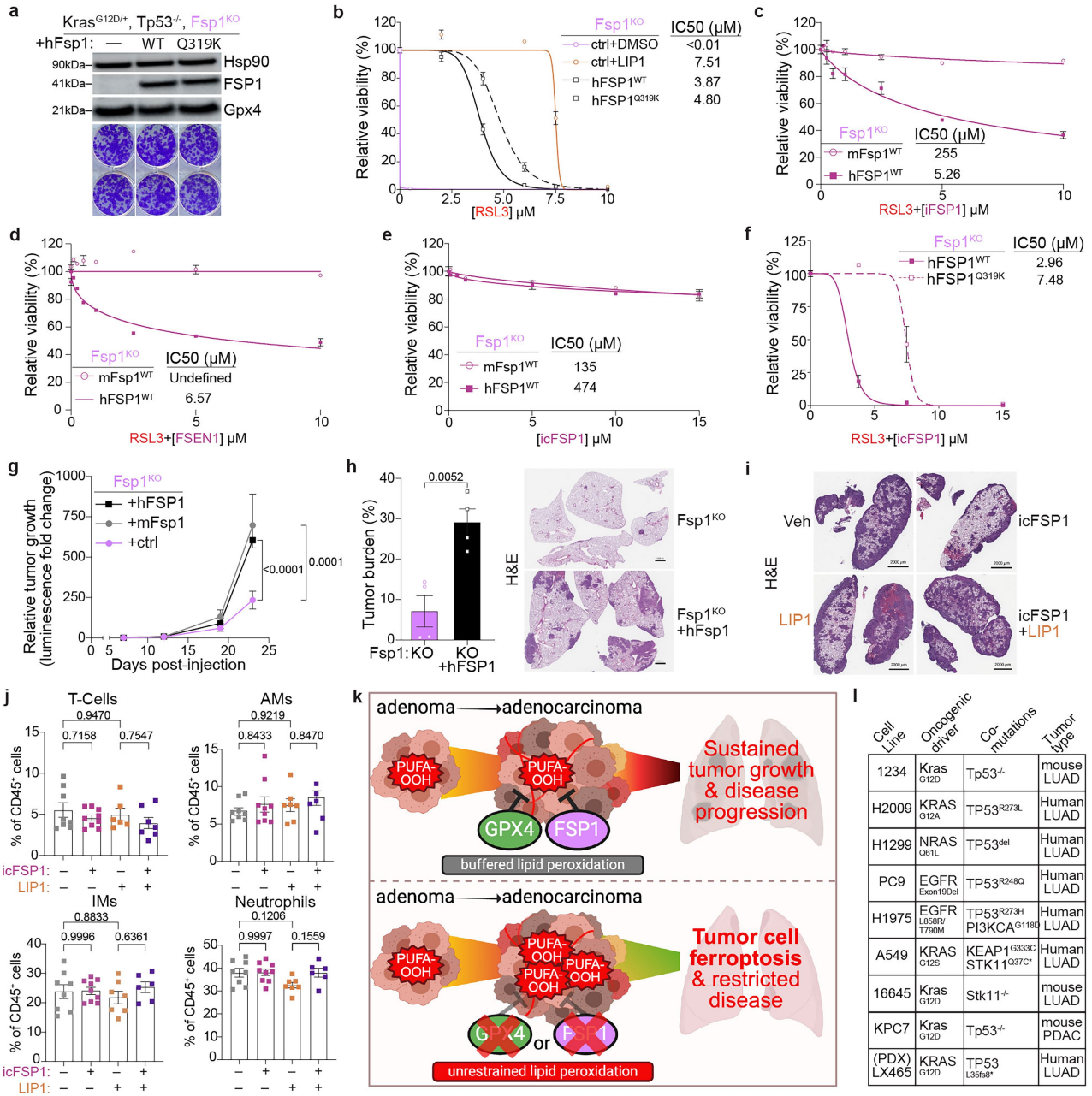

Cell Line	Oncogenic driver	Co-mutations	Tumor type
1234	Kras G12D	Tp53-/-	mouse LUAD
H2009	KRAS G12A	TP53R273L	Human LUAD
H1299	NRAS Q61L	TP53del	Human LUAD
PC9	EGFR Exon19Del	TP53R248Q	Human LUAD
H1975	EGFR L858R/ T790M	TP53R273H PI3KCAG1180	Human LUAD
A549	KRAS G12S	KEAP1G333C STK11Q37C*	Human LUAD
16645	Kras G12D	Stk11-/-	mouse LUAD
KPC7	Kras G12D	Tp53-/-	mouse PDAC
(PDX) LX465	KRAS G12D	TP53 L35fs8*	Human LUAD

Extended Data Fig. 7 | icFSP1 exerts on-target tumor-suppressive effect. **a**, Top: Western blot of KP, Fsp1^{KO} LUAD cells with re-expression of either empty vector (–), wildtype (WT) hFSP1, or Q319K-mutant hFSP1. Bottom: representative images of crystal violet clonogenic assay. **b**, Cell-TiterGlo Luminescence viability assay of KP, Fsp1^{KO} LUAD cells with re-expression of either empty vector (–), WT hFSP1, or Q319K-mutant hFSP1. **c**, CellTiter-Glo Luminescence viability assay of human or mouse Fsp1^{WT}-expressing cells upon RSL3 (0.2 µM) plus increasing concentrations of iFSP1. **d**, CellTiter-Glo Luminescence viability assay as in **c** but with FSEN1. **e**, CellTiter-Glo Luminescence viability assay of human or mouse Fsp1^{WT}-expressing cells upon increasing concentrations of icFSP1. **f**, CellTiter-Glo Luminescence viability assay of WT or Q319K-mutant hFSP1-expressing cells upon RSL3 (0.2 µM) plus increasing concentrations of icFSP1. **g**, Longitudinal tumour growth (measured via bioluminescence normalized to first imaging timepoint (day7)) in C57BL/6 J mice orthotopically transplanted with isogenic KP, Fsp1^{KO} cells with re-expression of either human FSP1 (hFSP1, n = 5), mouse Fsp1 (mFsp1, n = 6), or control (n = 6) vector. **h**, Tumour burden and representative H&E of KP, Fsp1^{KO} (n = 4) and hFSP1^{WT} (n = 4) orthotopic lung tumours. Scale bars: 1000 µm. **i**, Representative H&E of KP, hFSP1^{WT} orthotopic lung tumours from indicated treatment groups. Scale bar: 2000 µm. **j**, Percent of T cells, alveolar macrophages, interstitial macrophages, and neutrophils of total CD45+ cells in tumour bearing lungs from mice treated with the indicated compounds for two weeks (Veh, n = 8; LIP1, n = 7; icFSP1, n = 9; icFSP1 + LIP1, n = 6). **k**, Graphical summary depicting ferroptosis as a barrier to lung cancer, as loss of either Fsp1 or Gpx4 induces tumour cell ferroptosis and restricts disease progression. **l**, Summary table of cell lines, their respective tumour lineage, and mutations where Fsp1 loss resulted in tumour suppression in vivo. For all Cell-TiterGlo assays, n = 5 biological replicates per group. Data are represented as mean values, error bars represent SEM, significance determined via one-way ANOVA with multiple comparisons (panels **g**, **j**) or student's t test (panel **h**). For gel source data, see Supplementary Data 1. Drawings in **k** created in BioRender. Vaughan, A. (2025) https://BioRender.com/99qhixq.

nature portfolio

Corresponding author(s): Thales Papagiannakopoulos

Last updated by author(s): Aug 19, 2025

Reporting Summary

Nature Portfolio wishes to improve the reproducibility of the work that we publish. This form provides structure for consistency and transparency in reporting. For further information on Nature Portfolio policies, see our Editorial Policies and the Editorial Policy Checklist.

Statistics

For all statistical analyses, confirm that the following items are present in the figure legend, table legend, main text, or Methods section.

n/a	Confirmed
☐	☒ The exact sample size (*n*) for each experimental group/condition, given as a discrete number and unit of measurement
☐	☒ A statement on whether measurements were taken from distinct samples or whether the same sample was measured repeatedly
☐	☒ The statistical test(s) used AND whether they are one- or two-sided *Only common tests should be described solely by name; describe more complex techniques in the Methods section.*
☐	☒ A description of all covariates tested
☐	☒ A description of any assumptions or corrections, such as tests of normality and adjustment for multiple comparisons
☐	☒ A full description of the statistical parameters including central tendency (e.g. means) or other basic estimates (e.g. regression coefficient) AND variation (e.g. standard deviation) or associated estimates of uncertainty (e.g. confidence intervals)
☐	☒ For null hypothesis testing, the test statistic (e.g. *F*, *t*, *r*) with confidence intervals, effect sizes, degrees of freedom and *P* value noted *Give P values as exact values whenever suitable.*
☒	☐ For Bayesian analysis, information on the choice of priors and Markov chain Monte Carlo settings
☒	☐ For hierarchical and complex designs, identification of the appropriate level for tests and full reporting of outcomes
☒	☐ Estimates of effect sizes (e.g. Cohen's *d*, Pearson's *r*), indicating how they were calculated

Our web collection on statistics for biologists contains articles on many of the points above.

Software and code

Policy information about availability of computer code

Data collection	IVIS imaging was collected using Perkin Elmer Living Image Software 4.7.4. All cell viability and clonogenic assays were read on a Molecular Devices spectrophotometer. Imaging of Western Blots was carried out on a General Electric Amersham Imager 680. Mass spectrometry was performed on a Q Exactive Plus Quadrupole-Orbitrap (Thermo Fisher Scientific) equipped with a heated electrospray ionization (HESI) source and operated in negative ion mode. Flow cytometry was carried out using a BD LSRFortessa. IHC slides were scanned using a Hammamatzu Nanozoomer (2.0HT) and MultiIF images were acquired on Akoya Vectra Polaris (PhenoImagerHT) and uploaded to OMERO Plus image data management system (Glencoe).
Data analysis	All software are commercially or publically available. TCGA data were analyzed using R(v.3.3.2). GraphPad Prism v9.3 was used to plot and perform statistical analyses. IHC and other pathology images were analyzed using QUPath 0.5.4. LC/MS lipidomics was analyzed using Skyline (v24.1). Flow cytometry data was analyzed using FlowJO version 10.

For manuscripts utilizing custom algorithms or software that are central to the research but not yet described in published literature, software must be made available to editors and reviewers. We strongly encourage code deposition in a community repository (e.g. GitHub). See the Nature Portfolio guidelines for submitting code & software for further information.

Data

Policy information about availability of data

All manuscripts must include a data availability statement. This statement should provide the following information, where applicable:

- Accession codes, unique identifiers, or web links for publicly available datasets
- A description of any restrictions on data availability
- For clinical datasets or third party data, please ensure that the statement adheres to our policy

No original code was reported in this paper.
All data and raw gel images are included with the paper. Raw lipidomic data have been deposited in the MassIVE data base (https://massive.ucsd.edu/) under accession number MSV000098883. Analyzed lipidomic data are available in Supplementary Table 1. Gene expression profiles of primary tumors and relevant clinical data of 515 LUAD patients were obtained from The Cancer Genome Atlas6 (TCGute.org). GPX4, FSP1 (AIFM2), KRAS, EGFR, KEAP1, and STK11 mutational status of TCGA tumor samples was retrieved from cBioPortal151 using the TCGA PanCancer Atlas collection (gdc.cancer.gov/about- data/publications/pancanatlas). All other materials are available upon request from the corresponding author (T.P.). Source data are provided with this paper.

Research involving human participants, their data, or biological material

Policy information about studies with human participants or human data. See also policy information about sex, gender (identity/presentation), and sexual orientation and race, ethnicity and racism.

Reporting on sex and gender	n/a
Reporting on race, ethnicity, or other socially relevant groupings	n/a
Population characteristics	n/a
Recruitment	n/a
Ethics oversight	n/a

Note that full information on the approval of the study protocol must also be provided in the manuscript.

Field-specific reporting

Please select the one below that is the best fit for your research. If you are not sure, read the appropriate sections before making your selection.

☒ Life sciences ☐ Behavioural & social sciences ☐ Ecological, evolutionary & environmental sciences

For a reference copy of the document with all sections, see nature.com/documents/nr-reporting-summary-flat.pdf

Life sciences study design

All studies must disclose on these points even when the disclosure is negative.

Sample size	At least n=3 were used per condition for each in vitro experiment for statistical analysis. This indicates biological replicates which represent independently cultured cells. Formal power analyses were not calculated for in vitro experiments. At least n=4 were used per condition for each in vivo experiment. Sample sizes are indicated in figures/figure legends. For tumor experiments sample size was not calculated but was chosen in each experiment based on previous experience with various models and to ensure that there were enough samples to detect biologically relevant effects and to perform statistical analyses. For Flow cytometry at least 10,000 cells were quantified with each biological replicate.
Data exclusions	Values identified as extreme outliers by Grubbs' Test method were excluded.
Replication	All in vivo experiments were replicated at least twice with results reproducible of data shown in figures. When representative images are shown, a minimum of 3 samples from the larger cohort were stained from each group. In the case of representative MRI images, all animals from the cohort were imaged. All western blots were replicated at least 3 times with results reproducible of data shown in figures. All in vitro assays were replicated at least 3 times with a minimum of n=3 biological replicates per group for statistical power.
Randomization	Sample groups for in vitro experiments and lipidomics were allocated randomly. For relevant in vivo experiments mice were randomized into into treatment/dietary manipulation groups.
Blinding	During sample processing and analysis for the lipidomic the samples were given numeric IDs which after analysis, were unblinded and graphed. For histological and immunohistochemistry analysis, researcher was blinded to the sample condition. The investigators were not blinded during most other data collection or analysis. Data collection in all other experiments were collected in automated manner using indicated software. All processing conditions were applied uniformly.

Reporting for specific materials, systems and methods

We require information from authors about some types of materials, experimental systems and methods used in many studies. Here, indicate whether each material, system or method listed is relevant to your study. If you are not sure if a list item applies to your research, read the appropriate section before selecting a response.

Materials & experimental systems

n/a	Involved in the study
☐	☒ Antibodies
☐	☒ Eukaryotic cell lines
☒	☐ Palaeontology and archaeology
☐	☒ Animals and other organisms
☒	☐ Clinical data
☒	☐ Dual use research of concern
☒	☐ Plants

Methods

n/a	Involved in the study
☒	☐ ChIP-seq
☐	☒ Flow cytometry
☒	☐ MRI-based neuroimaging

Antibodies

Antibodies used

Gpx4 (Abcam) ab125066 1:2000
Fsp1 (Proteintech) 20886-1-AP 1:1000
Fsp1 14D7 Developed by Marcus Conrad 1:20
Acsl4 (Santa Cruz Biotechnologies) 271800 1:1000
pERK (Cell Signaling) #4370 1:2000
ERK (Cell Signaling) 4695 1:4000
Hsp90 (BD Biosciences) 610418 1:5000
4-HNE (JaICA) 1:200
Cleaved Caspase 3 Cell Signaling 1:400
KI67 Spring Bioscience, catalog no. M3062, 1:400
HRP-conjugated secondary antibody-ms ThermoFischer/Invitrogen 31430
HRP-conjugated secondary antibody-rb ThermoFischer/Invitrogen 65-6120
HRP-conjugated secondary antibody-rt ThermoFischer/Invitrogen 62-9520

Validation

Commerically available antibodies used in this study have been verified by the manufacturer and data can be found at the respective websites. In the case of the Fsp1 antibody from Marcus Conrad, he has verfied and published this antibody previously as cited in the text, and we verfied the antibody using WB of Fsp1 KO cells.

Eukaryotic cell lines

Policy information about cell lines and Sex and Gender in Research

Cell line source(s)

KP LUAD cell lines were obtained from the laboratory of Tyler Jacks.
16645 cell line was developed in T. P. Lab from KrasG12D LKB1-/- GEMM as previously described.
KPC7 cells were obtained from the laboratory of Diane Simeone.
H2009, H1299, PC9, H1975, A549 were purchased from ATCC.

Authentication

All mouse cell lines were authenticated by PCR genotyping. All human cell lines used were purchased from ATCC and were authenticated by short-tandem-repeat profiling.

Mycoplasma contamination

Cell lines tested negative for Mycoplasma every 6 month.

Commonly misidentified lines
(See ICLAC register)

No such cell lines were used

Animals and other research organisms

Policy information about studies involving animals; ARRIVE guidelines recommended for reporting animal research, and Sex and Gender in Research

Laboratory animals

C57BL/6J (JAX strain #000664)
Nude mice JAX strain #002019
NSG mice JAX strain #005557F
C57BL/6J Fsp1 KO (Conrad group)
All animals were aged 8 to 12 weeks when tumor studies began.

Wild animals

No wild animals were used

Reporting on sex	For subcutaneous data, male mice were used. For orthotopic lung tumor model, male mice were used unless specified in the legend section. For autochthonous GEMM, male and female mice were used.
Field-collected samples	No field-collected samples were used
Ethics oversight	All experiments were approved by the New York University (NYU) Institutional Animal Care and Use Committee (IA16-01627).

Note that full information on the approval of the study protocol must also be provided in the manuscript.

Plants

Seed stocks	n/a
Novel plant genotypes	n/a
Authentication	n/a

Flow Cytometry

Plots

Confirm that:

☒ The axis labels state the marker and fluorochrome used (e.g. CD4-FITC).

☒ The axis scales are clearly visible. Include numbers along axes only for bottom left plot of group (a 'group' is an analysis of identical markers).

☒ All plots are contour plots with outliers or pseudocolor plots.

☒ A numerical value for number of cells or percentage (with statistics) is provided.

Methodology

Sample preparation	Lung tissue was processed into a single cell suspension for flow cytometry as previously described43,55. Briefly, prior to euthanasia, mice were injected with 2 ug of Anti-mouse CD45-APC conjugated antibody (Biolegend, Clone 30-F11, 103111) retro-orbitally. Lungs were harvested and digested with Collagenase (Sigma-Aldrich, C5138) and deoxyribonuclease I (Sigma-Aldrich, DN25) followed by red blood cell lysis. Single cells were then resuspended in FACS buffer and stained using the following antibodies: CD45 (Biolegend, 103132), CD11b (Biolegend, 101216), CD11c (Biolegend, 117324), Ly6G (Biolegend, 127622), MHCII (BD, 748708), CD103 (Biolegend, 121433), CD64 (Biolegend, 139309), SiglecF (BD, 740956), MertK (R&D, BAF591), CD45 (BD, 748371), CD3e (BD, 740854), CD4 (Invitrogen, MCD0428), CD8a (EBioscience, 563152), Secondary (Streptavidin) (BD, 564176).
Instrument	BD LSR Fortessa
Software	BD FACSDiva 9.0 collection, FlowJo V10 analysis
Cell population abundance	N/A
Gating strategy	Gating is shown in supplemental figure 2. Cells were gated to exclude debris and doublets. Extravascular immune cells were identified by gating on CD45-PerCP-Cy5.5 positive and CD45-APC negative cells. T cells were identified as CD3e positive. Myeloid cells were identified as CD11b+ CD11c+. Neutrophils were gated on as Ly6G+ CD11b+. Of the remaining cells, eosinophils were excluded (SiglecF+ CD11b+). Macrophages were identified as CD64+ Mertk+. Macrophage subsets were gated on SiglecF+ CD11b- (Alveolar Macrophages) and SiglecF- CD11+ (Interstitial Macrophages).

☒ Tick this box to confirm that a figure exemplifying the gating strategy is provided in the Supplementary Information.